

**Endoscopic Time-Lapse Imaging of Immune Cells in Infarcted Mouse Hearts**  
Keehoon Jung, Pilhan Kim, Florian Leuschner, Rostic Gorbatov, Jun Ki Kim, Takuya Ueno,  
Matthias Nahrendorf and Seok Hyun Yun

*Circ Res.* 2013;112:891-899; originally published online February 7, 2013;  
doi: 10.1161/CIRCRESAHA.111.300484

*Circulation Research* is published by the American Heart Association, 7272 Greenville Avenue, Dallas, TX 75231  
Copyright © 2013 American Heart Association, Inc. All rights reserved.  
Print ISSN: 0009-7330. Online ISSN: 1524-4571

The online version of this article, along with updated information and services, is located on the  
World Wide Web at:

<http://circres.ahajournals.org/content/112/6/891>

Data Supplement (unedited) at:

<http://circres.ahajournals.org/content/suppl/2013/02/07/CIRCRESAHA.111.300484.DC1.html>

**Permissions:** Requests for permissions to reproduce figures, tables, or portions of articles originally published in *Circulation Research* can be obtained via RightsLink, a service of the Copyright Clearance Center, not the Editorial Office. Once the online version of the published article for which permission is being requested is located, click Request Permissions in the middle column of the Web page under Services. Further information about this process is available in the [Permissions and Rights Question and Answer](#) document.

**Reprints:** Information about reprints can be found online at:  
<http://www.lww.com/reprints>

**Subscriptions:** Information about subscribing to *Circulation Research* is online at:  
<http://circres.ahajournals.org/subscriptions/>

## Endoscopic Time-Lapse Imaging of Immune Cells in Infarcted Mouse Hearts

Keehoon Jung,\* Pilhan Kim,\* Florian Leuschner, Rostic Gorbatov, Jun Ki Kim, Takuya Ueno, Matthias Nahrendorf, Seok Hyun Yun

**Rationale:** High-resolution imaging of the heart *in vivo* is challenging owing to the difficulty in accessing the heart and the tissue motion caused by the heartbeat.

**Objective:** Here, we describe a suction-assisted endoscope for visualizing fluorescently labeled cells and vessels in the beating heart tissue through a small incision made in the intercostal space.

**Methods and Results:** A suction tube with a diameter of 2 to 3 mm stabilizes the local tissue motion safely and effectively at a suction pressure of 50 mm Hg. Using a minimally invasive endoscope integrated into a confocal microscope, we performed fluorescence cellular imaging in both normal and diseased hearts in live mice for an hour per session repeatedly over a few weeks. Real-time imaging revealed the surprisingly rapid infiltration of CX<sub>3</sub>CR1<sup>+</sup> monocytes into the injured site within several minutes after acute myocardial infarction.

**Conclusions:** The time-lapse analysis of flowing and rolling (patrolling) monocytes in the heart and the peripheral circulation provides evidence that the massively recruited monocytes come first from the vascular reservoir and later from the spleen. The imaging method requires minimal surgical preparation and can be implemented into standard intravital microscopes. Our results demonstrate the applicability of our imaging method for a wide range of cardiovascular research. (*Circ Res.* 2013;112:891-899.)

**Key Words:** circulation ■ imaging ■ leukocytes ■ monocyte ■ myocardial infarction

Acute myocardial infarction (MI) is the leading cause of morbidity and mortality worldwide. The human heart has a limited ability to self-repair damaged cardiac tissue. Therefore, a central theme in cardiovascular research is to understand a variety of cellular processes involved in the limited, yet important, natural healing processes and to develop strategies to overcome the problem. Chronic inflammation drives atherosclerosis progression,<sup>1</sup> and immune cells recruited after plaque ruptures<sup>2</sup> play significant roles in phagocytosis of dead or dying tissue, myofibroblast accumulation, angiogenesis, and deposition of collagen. Immune cells are also important factors in regenerative medicine, such as stem cell therapy and cellular reprogramming.<sup>3-5</sup> Despite the advances in molecular biology and genetics, our understanding of the recruitment and complex roles of immune cells at various stages of cardiovascular disease are limited. A new experimental technique that can significantly enhance our ability to investigate the complex and dynamic interaction of cardiovascular and immune systems in experimental animals

*in vivo* would have a high impact to the field of cardiovascular research, particularly for developing new therapeutic or preventive strategies for acute MI.

The mouse is a valuable *in vivo* model of human disease because of the availability of genetic tools and the similarity of the cardiovascular and immune system in the humans and mice. Current cardiovascular studies of mammalian hearts, however, have been hampered by the difficulty in examining various cellular events that occur in the heart *in vivo*.<sup>6,7</sup> Radiological whole-body imaging modalities, such as computed tomography and MRI, do not offer cellular-level resolution and sensitivity. Histology is a valuable tool, but this *ex vivo* analysis technique provides only static snapshot information of *in vivo* cellular processes, such as cellular trafficking and differentiation, that vary dynamically over time and heterogeneously in space. Over the past decade, intravital optical microscopy has emerged as a powerful tool in animal research. The high resolution and sensitivity of fluorescence microscopy, which cannot

Original received November 7, 2012; revision received February 4, 2013; accepted February 6, 2013. In January 2013, the average time from submission to first decision for all original research papers submitted to *Circulation Research* was 12.2 days.

From the Department of Dermatology, Wellman Center for Photomedicine (K.J., P.K., J.K.K., S.H.Y.) and Center for Systems Biology (F.L., R.G., T.U., M.N.), Harvard Medical School, Massachusetts General Hospital, Boston, MA; Graduate School of Nanoscience and Technology (WCU), Korea Advanced Institute of Science and Technology, Daejeon, Korea (P.K., J.K.K., S.H.Y.); The Harvard-MIT Division of Health Sciences and Technology, Cambridge, MA (S.H.Y.); Department of Internal Medicine III, University of Heidelberg, Heidelberg, Germany (F.L.); and DZHK (German Centre for Cardiovascular Research), Partner Site Heidelberg/Mannheim, Heidelberg, Germany (F.L.).

\*These authors contributed equally to this work.

The online-only Data Supplement is available with this article at <http://circres.ahajournals.org/lookup/suppl/doi:10.1161/CIRCRESAHA.111.300484/-DC1>.

Correspondence to Seok Hyun Yun, Harvard Medical School, Massachusetts General Hospital, 65 Landsdowne St Rm 525, Cambridge, MA 02139. E-mail syun@hms.harvard.edu

© 2013 American Heart Association, Inc.

*Circulation Research* is available at <http://circres.ahajournals.org>

DOI: 10.1161/CIRCRESAHA.111.300484

**Nonstandard Abbreviations and Acronyms**

<b>EGFP</b>	enhanced green fluorescence protein
<b>FOV</b>	field of view
<b>MI</b>	myocardial infarction

be achieved with radiological whole-body imaging, are critical for its widespread use in diverse research fields, including immunology, cancers, neuroscience, and stem cell biology.<sup>8–10</sup> Despite their earlier success with open-heart vasculature imaging,<sup>11</sup> scientists in cardiovascular research have been largely unable to benefit from this technology owing to the difficulty of obtaining minimally invasive access to the heart and owing to the motion artifacts induced by the heartbeat. To overcome these obstacles, several motion-correction techniques have been developed, including image registration,<sup>12,13</sup> temporal gating,<sup>14</sup> and motion-suppression devices, such as implanted windows, glue, and centimeter-wide suction rings.<sup>15</sup> Although each of these approaches has been useful for imaging specific tissues at micro to macroscopic resolutions, cellular imaging of the beating heart tissue poses a unique challenge because of the magnitude of the tissue movement and the micron-scale stabilization required for a subcellular resolution. In addition, the approach should be minimally invasive to enable repeated imaging for longitudinal studies.

We here present a miniature suction-assisted endoscope suitable for imaging cellular events in the beating heart of the mouse. The endoscope uses a suction tube device that can locally stabilize the tissue underneath it without causing detrimental effects and permits cellular-level imaging. The endoscope can achieve access to the outer surface of the heart through a small incision made in the skin and in the intercostal muscle between the ribs without breaking the bones. We have previously reported *in vivo* imaging of the beating heart and cardiac grafts transplanted in the abdominal cavity using similar optical probes.<sup>16</sup> The endoscopic approach solves the problem of the more invasive open-heart microscopy demonstrated by Li et al.<sup>17</sup> Our approach is distinctly different from the recent technique demonstrated by Lee et al,<sup>18</sup> where a small-diameter objective lens was firmly glued onto the heart tissue. The fixation of the lens not only limits the field of view (FOV) but also can cause considerable perturbations. Thus far, none of the previous techniques allowed repeated, time-lapse imaging of the heart tissue. We report here an imaging technique enabling minimally perturbed, longitudinal imaging of the heart. We demonstrate repeated imaging of immune cells and vessels in normal healthy hearts over a period of weeks and of monocytes circulating in the blood and infiltrating in infarcted hearts. As an application of this unique capability, we performed an *in vivo* imaging study with a mouse model of acute MI. We measured the numbers of monocytes at various locations in the heart from the onset of MI. Quantitative image analysis revealed unexpected kinetics in the monocyte infiltration in the very early phase of MI within minutes after occlusion. Our study provides fresh insights into the time-dependent origins of the monocytes that infiltrate into infarcted myocardium.

**Methods****Optical Probe**

The imaging core was fabricated in house by attaching 3 graded-index rod lenses (Models: ILW-1/4 pitch, SRL-1/2 pitch, and ILW-1/4 pitch, NSG America, Inc.).<sup>19–21</sup> The triplet lens endoscope was then reinforced with a stainless steel metal sleeve (OD=1.25 mm). The probe had a  $\times 1$  magnification and a length of 20 mm. The suction tube was fabricated by cutting stainless steel tubing (NSG America). The smaller tube had diameters of 1.4 mm (ID) and 1.8 mm (OD), and the larger one was 2.7 mm (ID) and 2.9 mm (OD). The lens probe was inserted into the suction tube through a small cut made in the side of the latex rubber tubing (ID=1.8 mm). The incision was closed automatically by the elasticity of the rubber, which seals the suction channel. The rubber tube was connected to a miniature vacuum pump (NF5, KNF Nueberger) via a vacuum gauge, a liquid absorber, and a valve. UV epoxy was applied to the bottom of the suction tube to form an epoxy O-ring, which tightened the vacuum seal and protected the tissue. The imaging platform was a previously described custom-built video-rate confocal fluorescence microscope previously described.<sup>22,23</sup> The system acquired 3-color images (512 $\times$ 512 pixels) at 30 frames per second. The images are displayed in real time on a computer monitor and streamed to a hard disk. The custom data acquisition program can also display and record images averaged over an arbitrary number of consecutive frames in real time.

**Measurement of the Effects of Suction**

We used a standard rigid-body translational motion correction algorithm based on cross-correlation<sup>24</sup> to calculate the amplitude and the direction of the shift between individual frames (Figure 1B). The peak-to-peak shift during the heartbeat was used as the metric to measure the amount of tissue motion as a function of the suction pressure. The motion information was also used to align individual frames to reduce the residual motion artifacts by frame averaging (over 1–3 seconds) to enhance the signal:noise ratio and to make large-area mosaic images.<sup>23</sup> This software correction method was effective only once the tissue motion was reduced to less than a few tens of microns. To measure blood flow, we injected fluorescently labeled red blood cells (or polystyrene micro beads) intravenously and analyzed the number of flowing cells per second and their speeds in the bloodstream from the acquired video images. Red blood cells were isolated from a mouse and stained with DiI fluorescent dye. The blood pressure and heart rate were measured with a CODA monitor (Kent Scientific, Computed tomography) using a volume pressure sensor with a mouse-tail cuff.

**Animals**

B6.129P-Cx<sub>3</sub>cr1<sup>m1Lit/J</sup> (Cx<sub>3</sub>cr1<sup>sgfp/sgfp</sup>) mice<sup>25</sup> (Jackson Laboratories) and *LysM*<sup>sgfp/sgfp</sup> mice<sup>26</sup> were obtained. Cx<sub>3</sub>cr1<sup>sgfp/+</sup> mice were generated by breeding Cx<sub>3</sub>cr1<sup>sgfp/sgfp</sup> mice with C57BL/6J mice. Cx<sub>3</sub>cr1<sup>sgfp/+</sup> mice have 1 Cx<sub>3</sub>cr1 allele replaced with cDNA encoding enhanced green fluorescence protein (*Egfp*) and were used to track monocytes. *LysM*<sup>sgfp/+</sup> mice have 1 *LysM* allele replaced with cDNA encoding *Egfp* and were used to track neutrophils. *Major histocompatibility complex-II*<sup>sgfp/+</sup> mice expressing the major histocompatibility complex class II molecule infused into EGFP were used to visualize antigen-presenting cells. *Tie2*<sup>sgfp/+</sup> mice expressing the Tie2 receptor infused into EGFP were used to visualize blood endothelial cells. The mice were 8 to 10 weeks old. The institutional subcommittee on research animal care at Massachusetts General Hospital approved all animal studies.

**Animal Model of MI**

Each mouse was anesthetized with inhalational isoflurane before preoperative skin preparation. The thorax was shaved using electric clippers. Betadine solution was applied to the shaved area and allowed to dry. The mouse was placed on a plate heated by a silicone rubber heater to maintain the body temperature. Once the mouse was fully anesthetized, it was intubated and mechanically ventilated with oxygen supplemented with 2% isoflurane. The mouse underwent a thoracotomy in the fourth left intercostal space to obtain access to the heart, and the infarct was created by permanent ligation of the left anterior descending coronary artery.

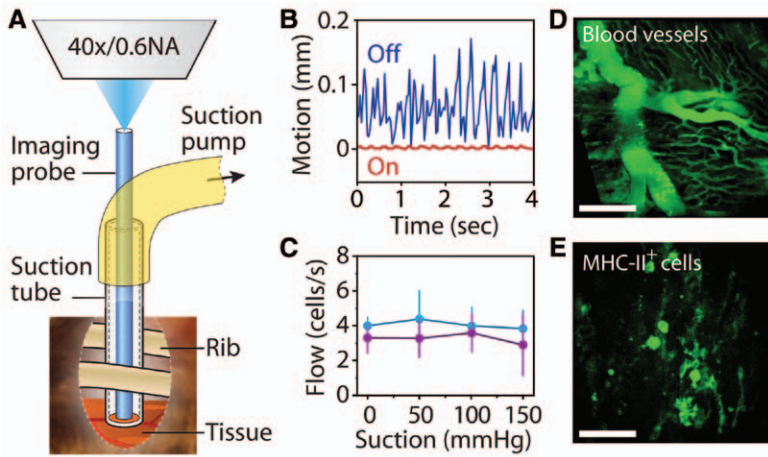


**Figure 1. Motion-stabilizing endomicroscopy.** **A**, Schematic of suction-assisted endoscopy. **B**, Horizontal shifts of the heart tissue with suction (red curve) at a pressure of 50 mmHg and without suction (gentle pressure was applied; blue curve) measured from cross-correlation analysis of a movie. The tissue movement was reduced to 3  $\mu$ m by suction. **C**, The number of cells flowing per second in the bloodstream in 2 different vessels (blue and purple circles) in the renal capsule at suction pressure levels from 0 to 150 mmHg. **D**, Images of blood vessels on the anterior surface of the heart in vivo. The vessels are visualized by intravenously injected fluorescein-isothiocyanate-Dextran. **E**, Images of major histocompatibility complex (MHC) class II<sup>+</sup> antigen-presenting cells in a *MHC-II<sup>gfp/+</sup>* mouse in vivo. **D, E**, The image is an average of 90 frames acquired in 3 seconds ( $\approx$ 23 heart beats), and scale bars indicate 50  $\mu$ m.

**In Vivo Heart Imaging**

A 3-axis translation stage was used to move the mouse so that the center of the laser scanning pattern emitted from the endoscope was aligned with the tissue incision made in the chest. The suction valve was initially open (ie, a suction pressure of 0 mmHg). Once the probe made an initial contact with the heart tissue, the animal stage was moved up slightly (0.6–0.8 mm) to induce gentle physical pressure on the tissue underneath the endoscope. The suction valve was then closed slowly until the suction pressure reached to the desired level. Once the suction was established, the animal stage was lowered slowly to confirm stable suction of the tissue by the suction tube and to minimize or prevent potential tissue damage from the additional mechanical pressure applied before suction. For wide-area imaging, the mouse stage was translated in the horizontal direction to move the tissue and the suction tube together. Fluorescence movies were recorded continuously during the scan. Once the scan was completed over an area, large-area images were obtained using mosaic registration. We used a suction tube with a sufficiently long length (15.2 mm) so that the tube tilted easily with a small torque and the maximum tilt angle was small ( $<2^\circ$ ). The suction pressure was maintained during translation owing to the deformation of the elastic rubber tube that connects the suction tube and the optical probe. The focal plane in the tissue was adjusted remotely by controlling the distance of the microscope objective to the imaging probe. To visualize the blood vessels, 100  $\mu$ L of tetramethylrhodamine-isothiocyanate-Dextran (5 mg/mL) was injected intravenously and excited at 532 nm. Alternatively, fluorescein-isothiocyanate-Dextran was used and excited at 491 nm.

**Cell Counting and Cellular Perfusion Rate**

To determine the number of CX<sub>3</sub>CR1<sup>+</sup> or LysM<sup>+</sup> cells, images were acquired at  $\approx$ 30 to 50 different arbitrarily chosen sites with a FOV of 250  $\mu$ m each. At each imaging site, z-stack images were acquired at the depths from 0 to 100  $\mu$ m by changing the imaging plane. The image acquisition took  $\approx$ 2 minutes ( $\pm$ 1 minutes) at each time point (n=3–5). The number of cells was counted with an image segmentation algorithm based on the brightness and sizes of the fluorescent objects. The average number of cells was counted and divided by the image volume (ie, 250 $\times$ 250 $\times$ 100  $\mu$ m<sup>3</sup>) to calculate the cell density per milligram (or 1 mm<sup>3</sup> in volume) of tissue. The number of flowing and rolling cells in the blood vessels was counted manually from the acquired video-rate movies. The cellular perfusion rate, or flux, was defined as the total number of moving cells per unit volume per unit time (ie, divided by the recording time period).

**Immunohistochemistry and Flow Cytometry**

For histological analysis, tissues were harvested from the heart of the *Cx<sub>3</sub>cr1<sup>gfp/+</sup>* mice before and after MI at day 5 and prepared for frozen sections. We also performed MI surgery or sham surgery on C57BL/6J wild-type mice and harvested the heart tissues from various regions after applying different suction pressures. The sections were stained with anti-CD11b or anti-green fluorescent protein

antibody and counterstained with DAPI to observe the nuclei. For the flow cytometry, the heart and spleen tissues were harvested from the control and the MI mice. The tissues were digested in an enzyme mixture and passed through a cell strainer. The single cell suspensions were stained with the following antibodies: CD11b-APC-Cy7, B220-PE, CD49b-PE, CD90-PE, Ly-6G-PE, NK1.1-PE, Ter119-PE, and F4/80-PE-Cy7 (BD Biosciences). Monocyte subsets were identified as CD11b<sup>high</sup> (B220/CD49b/CD90/Ly-6G/NK1.1/Ter119)<sup>low</sup> F4/80<sup>low</sup>. The flow cytometry was performed using a multicolor flow cytometer (FACSAria, BD Biosciences).

**Statistical Analysis**

The measured values were presented as mean $\pm$ SD. *P* values were calculated using the Student–Newman–Keuls test. A difference is considered significant when *P* $<$ 0.05.

**Results**

**Miniature Suction Endoscope**

The endoscope consisted of a lens probe and an outer suction tube (Figure 1A). The probe was made of triplet graded index lenses<sup>21,27</sup> with an OD of 1 mm and a stainless steel sleeve with an OD of 1.25 mm. The assembled probe was integrated into a real-time laser-scanning confocal microscope<sup>22</sup> using mechanical mounts<sup>19</sup> (Online Figure I). The graded index lens probe had a typical resolution of 1  $\mu$ m in the lateral dimension and 10  $\mu$ m in the axial dimension, a typical penetration depth of up to 100  $\mu$ m, and an intrinsic FOV of 250  $\mu$ m (approximately a quarter of the diameter of the graded index lens).<sup>21</sup> The probe was inserted into a stainless steel suction tube through a small incision made in a rubber tube that connects the suction tube to a microdiaphragm pump. The suction system used a vacuum gauge, a flow valve, and a liquid absorber (Online Figure II). We used 2 different suction tubes. The narrower tube had 1.8 mm OD and 1.4 mm ID, and the larger suction tube, which was used for wide area imaging, had an OD of 2.9 mm and an ID of 2.7 mm. Either tube was sufficiently thin to be inserted through a small incision (2–6 mm) made in the intercostal space.

**Suction-Assisted Motion Stabilization**

During the cardiac cycle, the surface of the heart normally moves up to 1 to 2 mm in both the vertical and lateral directions (Online Video IA). It was possible to suppress much of the tissue movement by pressing the tissue surface with the flat surface of the lens probe. However, the residual movement,

typically  $>100\ \mu\text{m}$ , is too large to avoid significant blurring (owing to lateral motion) and blinking artifacts (owing to vertical motion; Online Videos I). In principle, the movement can be further decreased with increasing pressure to achieve micron-scale stabilization, but such attempts almost always result in a complete blockage of the blood flow and apparent tissue damage within a few minutes.

We have found that suction is generally a safer and more effective method for mechanical stabilization. After positioning our endoscope above the target tissue, we moved the animal stage up while monitoring the real-time fluorescence images until the physical contact between the tissue and the lens probe was steady. Once the desired suction pressure level was reached and the movement was suppressed, the animal stage was lowered slightly to avoid the potential tissue damage caused by sustained physical pressure. We found that a suction pressure of 50 mmHg reduces the movement of the heart tissue to  $<5$  to  $10\ \mu\text{m}$  (Figure 1B; Online Videos I). For abdominal organs, such as the kidney, spleen, liver, and intestine, 50 mmHg was sufficient to restrict the tissue motion to  $<2$  to  $5\ \mu\text{m}$  (Online Figure III). Once the movement is reduced to  $<10\ \mu\text{m}$ , motion correction by image registration can be used to reduce the residual motion artifacts. The total suction force exerted on the tissue by a 1.8-mm tube was calculated to be only 0.6 mN at 50 mmHg. When a 2.9-mm tube is used, the estimated suction force was 33 mN, which is equivalent to a weight of only 3.4 g distributed on an area of  $5\ \text{mm}^2$  (Online Video II).

### Effect of Suction on Local Blood Perfusion

The applied suction pressure was in fact comparable with the normal arterial blood pressure ( $\approx 120\ \text{mmHg}$ ) driving the blood flow. To investigate the effect of the suction on the local perfusion, we injected DiI-labeled red blood cells into the tail vein and measured their flowing speed in the bloodstream in both the heart and the kidney where the measurement of baseline flow was possible without the suction pressure. At a suction pressure of up to 100 mmHg, no apparent changes in the flow were observed compared with the baseline at 0 mmHg (Figure 1C; Online Figure VI). As the pressure was increased to 150 mmHg, the blood flow in the small capillaries near the tissue surface began to be compromised. At a pressure  $>150\ \text{mmHg}$ , a noticeable reduction in the flow speed was observed in the heart and in other organs (Online Videos III). Because the suction-induced external pressure within the tissue decreases quickly with depth, we expected that for the vessels located beyond the imaging depth (ie,  $>100\ \mu\text{m}$ ), the blood flow would be intact even at 150 mmHg.

Once the local tissue is held stably, the focal plane of the endoscope can be remotely adjusted by simply translating the axial position of an objective lens using a microtranslational stage.<sup>21,27</sup> The suction-assisted endoscope allowed us to visualize the microvasculature and the individual cells in the beating heart (Figure 1D and 1E) and in the breathing lung with minimal motion artifacts (Online Figure V).

### Minimal Perturbation of Normal Physiology

To determine whether the suction produces any undesirable influence on the cardiac physiology, we measured the blood

pressure and the heart rate of mice ( $n=4$ ) using a tail cuff sensor during imaging. The measured systolic blood pressure was  $120\pm 3\ \text{mmHg}$ , and the diastolic blood pressure was  $91\pm 2\ \text{mmHg}$ , independent of the suction pressure as it varied from 0 to 300 mmHg (Online Figure VI). The measured heart rate was also invariant at  $457\pm 11\ \text{bpm}$ , independent of a suction pressure of up to 300 mmHg (Online Figure VII). We also examined the histological tissue sections obtained after prolonged suction for 1 hour at 50 mmHg and observed no signs of tissue damage. Only at an extreme suction level of 300 mmHg was minor hemorrhaging observed (Online Figure VIII). Finally, we performed immunohistochemistry analysis and confirmed that suction did not induce inflammation (Online Figure IX). All of our measurements suggest that local suction at 50 to 100 mmHg causes minimal perturbations to the heart, both at the local tissue and at the organ levels.

### Wide-Area Scan Using a Suction Tube

Once the suction tube is placed at a specific location, it is possible to scan a wider area than the intrinsic FOV ( $250\ \mu\text{m}$ ) of the probe. We achieved the scanning by moving the tissue and the suction tube with respect to the lens probe fixed to the microscope head by controlling the mouse stage with a motorized translation stage (Figure 2A; Online Figure X). The maximum scan area is a circle with a diameter of 1.7 mm (equal to the ID of the 2.9-mm tube minus the OD of the probe plus the intrinsic FOV; Figure 2B). The tissue can be moved in the horizontal direction continuously in a raster or other scan pattern (Online Video IV). Alternatively, images can be obtained at discrete locations with some overlap (typically

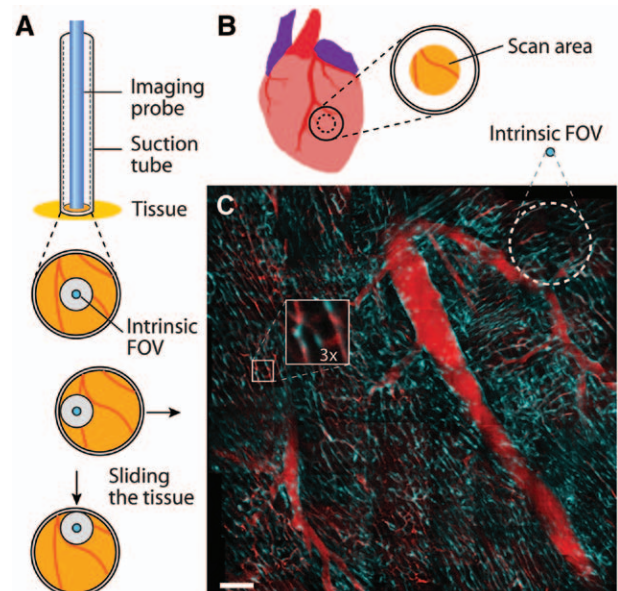


**Figure 2. Wide-area imaging.** **A**, Illustration of scanning operation. Moving the suction tube and the tissue with respect to the stationary probe changes the imaging site. **B**, Schematic of the heart and the maximum scan area for a given tube diameter. **C**, A mosaic image of the blood vasculature on the left ventricle of the heart visualized using green fluorescent protein in  $\text{Tie}2^+$  cells (cyan pseudo color) and intravenously injected anti-CD31 antibody conjugated with Alexa 647 (red pseudo color). Suction pressure, 50 mmHg. The dotted circle (white) indicates the  $250\text{-}\mu\text{m}$  field of view (FOV) of the lens probe. **Inset**,  $3\times$  enlarged view. The image spans  $1.2\ \text{mm}$  by  $1.2\ \text{mm}$ . Scale bar,  $100\ \mu\text{m}$ .

>30%) between the adjacent frames and converted to a mosaic by image processing. Using this stepwise scan, we acquired several hundred images of the coronary vasculature in a *Tie2<sup>slp/+</sup>* mouse with double fluorescent staining and obtained a 2-color mosaic image spanning an area of 1.2 mm by 1.2 mm (a diagonal length of 1.7 mm; Figure 2C).

### Longitudinal Heart Imaging

A compelling advantage of minimally invasive endoscopic imaging is the ability to visualize the same tissue site repeatedly over the course of time. Longitudinal heart imaging is challenging because excessive perturbation to the vital organ and the chest cavity can easily cause complications, leading to the death of the animal. To demonstrate repeated time-lapse imaging, we used *Cx<sub>3</sub>cr1<sup>slp/+</sup>* knock-in mice,<sup>25</sup> in which CX<sub>3</sub>CR1<sup>+</sup> cells express the EGFP. The CX<sub>3</sub>CR1<sup>+</sup> cells in the bloodstream are predominantly monocytes, although the fractalkine receptor is also expressed by other rare leukocytes.<sup>28,29</sup> We imaged CX<sub>3</sub>CR1<sup>+</sup> cells in the heart of a *Cx<sub>3</sub>cr1<sup>slp/+</sup>* mouse at intervals of 1 to 10 days. At the completion of each imaging session, the chest incision was closed with a suture, and the animal was kept in the cage until the next imaging session. The above-described scanning method was used to locate the same region, which was defined using the vasculature pattern as a landmark (Figure 3). During each imaging session, which typically lasted no more than an hour, we observed many round-shaped CX<sub>3</sub>CR1<sup>+</sup> monocytes flowing, rolling, or crawling in the blood vessels, and very few of the cells were found outside the vessels. We also observed virtually stationary monocytes during each imaging session, almost all of which were located in the blood vessels (Figure 3D). The density of these stationary CX<sub>3</sub>CR1<sup>+</sup> cells was measured to be  $\approx 1000$  cells/mm<sup>3</sup> (ie, per milligram of tissue). The longitudinal images show that these stationary cells actually move over the course of days. Nevertheless, there was no apparent change in the average number or the morphology of these cells in the span of 2 weeks, which indicates that our imaging procedure did not induce any significant inflammatory response.

### Imaging Tissue-Resident Myeloid Cells

We imaged various tissues in different organs in *Cx<sub>3</sub>cr1<sup>slp/+</sup>* mice and in *LysM<sup>slp/+</sup>* mice<sup>26</sup> in the normal physiological condition. Compared with the low population of CX<sub>3</sub>CR1<sup>+</sup> monocytes in the heart, CX<sub>3</sub>CR1<sup>+</sup> cells were found in much

higher density in the spleen and the lung (Online Figure XIA). The CX<sub>3</sub>CR1<sup>+</sup> monocytes in the spleen had an approximately roundish morphology. In contrast, most of the CX<sub>3</sub>CR1<sup>+</sup> cells (presumably nonmonocytes) in the lung and the liver had non-round irregular shapes (Online Figure XIB). In the *LysM<sup>slp/+</sup>* mice, the density of LysM<sup>+</sup> neutrophils<sup>26</sup> was also high in the spleen and the lung but low in the heart and the liver (Online Figure XIC). Most of the LysM<sup>+</sup> cells had round shapes in all the organs examined (Online Figure XID).

### Monocyte Infiltration After Acute MI

We used the imaging method to study the infiltration of immune cells into the heart after acute MI. To induce acute MI, we ligated the left anterior descending coronary artery. In *Cx<sub>3</sub>cr1<sup>slp/+</sup>* mice at 3 hours after the ligation, we observed a dramatic increase of CX<sub>3</sub>CR1<sup>+</sup> cells in the infarcted area, whereas a remote site maintained the normal population level (Figure 4A). In the remote site, most monocytes were round and present in the blood vessels, as in the control and sham-operated mice. In the infarcted region, many monocytes were observed, and most of the cells had spiky shapes and was apparently located outside the occluded blood vessels (Figure 4B). The border area had both spiky cells in the tissue and round monocytes in the bloodstream (Online Figures XII and XIII). To visualize monocytes immediately after the onset of MI, we also performed the ligation in situ while the animal was imaged with the endoscope. Time-lapse imaging revealed the kinetics of early monocyte infiltration (Figure 5A). The number of CX<sub>3</sub>CR1<sup>+</sup> cells in the infarct increased from 1000 to 5000 cells/mg of tissue in 5 minutes and to 10000 cells in 30 minutes. Repeated imaging sessions on days 1 and 6 showed that the number of cells increased continuously but at reduced rates, whereas the cell number in the remote site did not change significantly until 1 day after MI (Figure 5B; Online Figure XIV).

In the *LysM<sup>slp/+</sup>* mice after acute MI, the number of LysM<sup>+</sup> neutrophils reached its maximum on day 1 and decreased gradually afterward (Figure 5C and 5D), consistent with previous results obtained by flow cytometry.<sup>33</sup> There was no obvious difference between the morphology of the neutrophils at the infarct and the remote sites. During the initial 30 minutes after MI, the rate of increase of monocytes outpaced those of neutrophils (Figure 5E), which is contrary to the prevailing conventional notion that the recruitment of monocytes is preceded by that of neutrophils in MI.<sup>2</sup>

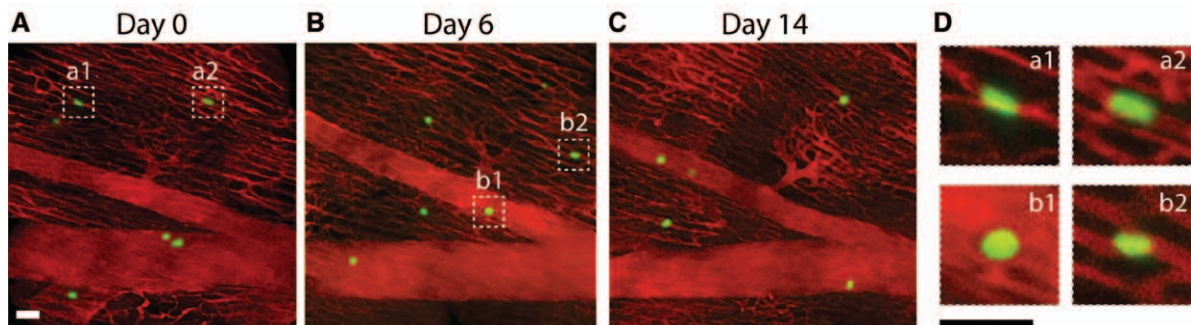


**Figure 3. Longitudinal imaging.** **A** to **C**, Images of CX<sub>3</sub>CR1<sup>+</sup> cells (green) and blood vessels (red) in the same region of the heart of a *Cx<sub>3</sub>cr1<sup>slp/+</sup>* mouse, acquired at 3 imaging sessions: **A**, day 0; **B**, day 6; and **C**, day 14. **D**, Enlarged images of the small areas marked by dotted squares in **A** and **B**. Scale bars, 50  $\mu$ m.

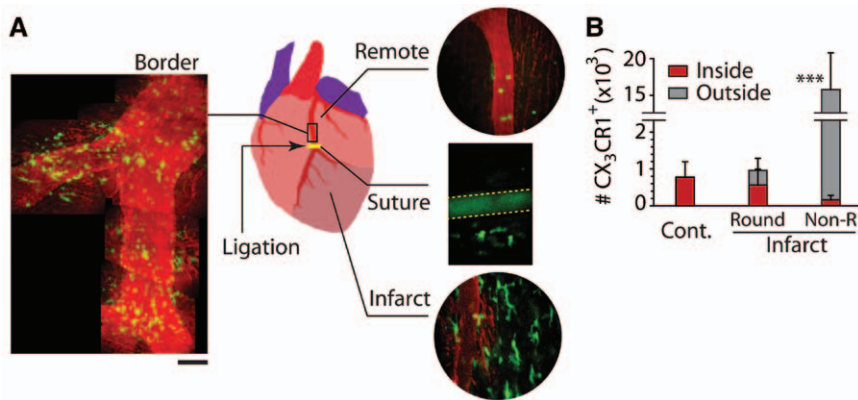


**Figure 4. Analysis of various regions of infarcted myocardium.** **A**, Schematic of infarcted heart and fluorescence images of various regions. Images show CX<sub>3</sub>CR1<sup>+</sup> monocytes (green) and blood vessels (red) at 3 hours post-myocardial infarction (MI) in the border, remote, and infarct areas, and at the boundary of the infarct, indicated by the autofluorescence of the suture (yellow dotted lines) used for ligation. **B**, Number of CX<sub>3</sub>CR1<sup>+</sup> monocytes per milligram of tissue recruited into the infarct at 3 hours post-MI. Round cells are defined as cells with circular or elliptical shapes with an aspect ratio of <3:1. Nonround cells have aspect ratios >3:1. Cells overlapping with a vessel by more (less) than 80% were considered to be inside (outside) the vessel. Error bars, SD (n=3–5). Scale bars, 50 μm. \*P<0.05; \*\*P<0.01; \*\*\*P<0.001 vs control.

**Imaging Rolling and Flowing Monocytes in the Circulation**

It is well known that inflammatory monocytes infiltrate ischemic tissue early after MI,<sup>2</sup> but the massive recruitment we observed within minutes after the onset of ischemia was unexpected. To determine the origin of the cells, we examined the CX<sub>3</sub>CR1<sup>+</sup> monocytes in the bloodstream more carefully. In the normal state, video-rate imaging showed the monocytes rapidly flowing in coronary arterioles at a typical speed of 2 mm/s. In the coronary venules, we observed cells flowing at a speed of 0.4 to 1.2 mm/s. In addition to these flowing cells, we found many monocytes rolling (15–50 μm/s) or crawling (<15 μm/s) along the vessel walls (Figure 6A; Online Video V). To our knowledge, this is the first time patrolling behavior of monocytes is reported in the heart. Although rarely seen, some flowing cells exhibited rod shapes (with an aspect ratio up to 4:1) elongated in the direction of the flow (Figure 6B; Online Figure XV). The flux or perfusion rate of the flowing and the rolling monocytes was equivalent to a supply of ≈3000

and 2500 cells, respectively, per minute per 1 mg of tissue in both the control and the sham-operated animals (Figure 6C and 6D). It is interesting to find so many rolling monocytes, which are presumably patrolling during steady-state immune surveillance,<sup>28</sup> in the coronary vessels in the normal state without any stimulus. We calculated that the combined flux rates of flowing and rolling monocytes were sufficient to account for the rapid increase in the number of monocytes in the infarct after acute MI (Figure 5E). From these results, we hypothesized that the patrolling monocytes<sup>28</sup> in the circulation are the primary source of the monocytes found in the infarct immediately after the MI, and we further investigated this possibility.

**Origin of Early-Infiltrating Monocytes**

We found that after the onset of MI, both the absolute and relative numbers of flowing and rolling monocytes change considerably in the border area (Figure 6C and 6D). The perfusion rate of flowing monocytes increased significantly and continuously for 1 hour, whereas the number of rolling monocytes

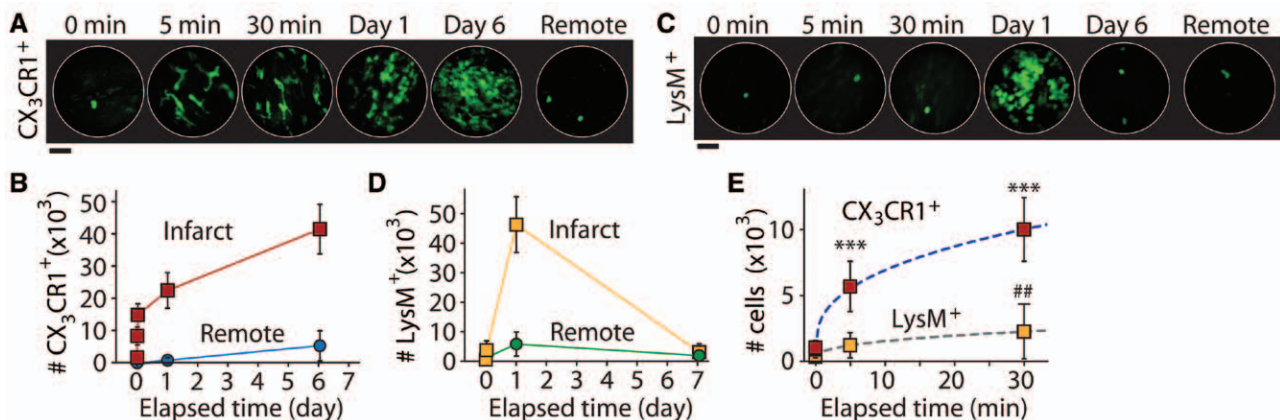


**Figure 5. Quantification of immune cell infiltration into myocardial infarct.** **A**, Images showing the infiltrated CX<sub>3</sub>CR1<sup>+</sup> monocytes, acquired from a *Cx<sub>3</sub>cr1<sup>gfp/+</sup>* mouse in 3 imaging sessions on day 0 (0–30 min), day 1, and day 6 post-MI. **B**, Number of CX<sub>3</sub>CR1<sup>+</sup> cells in the infarct (red) and remote (blue) areas. **C**, Time-lapse images of LysM<sup>+</sup> neutrophils in the heart tissue in a *LysM<sup>gfp/+</sup>* mouse in 3 imaging sessions on day 0, day 1, and day 6 post-MI. **D**, Number of neutrophils in the infarct (yellow) and remote (green) areas. **E**, Number of infiltrated monocytes (red squares) and neutrophils (orange squares) immediately after acute myocardial infarction (MI). Dotted line, curve fit based on power dependence on time ( $\alpha t^{0.38}$ ). Error bars, SD (n=3–5). Scale bars, 50 μm. \*P<0.05; \*\*P<0.01; \*\*\*P<0.001 vs 0 min. #P<0.05; ##P<0.01 vs 0 min.

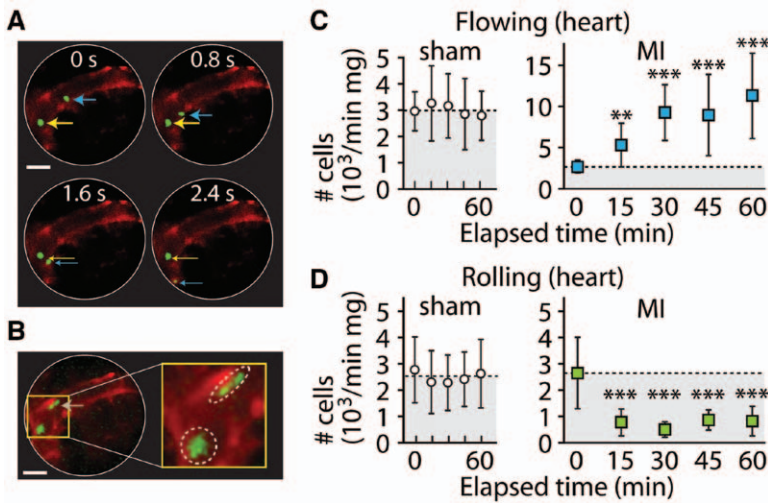


**Figure 6. Flowing and rolling monocytes in normal and infarcted hearts (border).** **A**, Movie frames showing monocytes rolling (cyan arrow) and crawling (yellow arrow) in a coronary venule (red, visualized by tetramethylrhodamine-isothiocyanato-Dextran) in the heart tissue. **B**, Trace of rod-shaped monocytes flowing in the coronary venule. Scale bars, 50  $\mu\text{m}$  in **A** and **B**. **C**, Flux of flowing monocytes in circulation in the heart after sham operation (sham; left) and after acute myocardial infarction (MI; right). **D**, Flux of rolling monocytes in blood vessels in the sham-operated (left) and infarcted (right) hearts. Error bars, SD (n=3–5). \* $P < 0.05$ ; \*\* $P < 0.01$ ; \*\*\* $P < 0.001$  vs 0 min.

decreased significantly. The rapid transition from rolling to flowing might be a mechanism to accelerate the infiltration into the infarct. The number of flowing monocytes tripled after 30 minutes, suggesting the onset of monocytes from a second source, which is most likely the spleen.<sup>30,31</sup>

We also measured the number of monocytes in the peripheral vessels in the skin (Online Video VI). The perfusion rates of flowing and rolling CX<sub>3</sub>CR1<sup>+</sup> cells were  $\approx 5000$  and 6000 cells/min per milligram, respectively, in both the control and the sham-operated animals (Figure 7A and 7B). These rates decreased by nearly 50% at 15 to 30 minutes after MI but recovered to the normal levels after 60 minutes (Figure 7A and 7B). The initial depletion of the circulating monocytes could be caused by their recruitment into the infarcted heart tissue. The subsequent replenishment was attributed to the release of monocytes from the spleen.<sup>31</sup>

The results suggest that the monocytes at the infarct site are first recruited from the vascular pool and then from the splenic reservoir after 15 to 30 minutes, which is much earlier than previously thought.<sup>31</sup> To support this conclusion, we performed flow cytometry with the tissues harvested as early as 3 hours post-MI and measured an  $\approx 10$ -fold increase in the number of monocytes in the infarcted region and a considerable decrease in monocytes ( $\approx 200\,000$  cells) in the spleen (Online Figure XVI). We used conventional immunohistochemistry to confirm the increase of the monocytes in the heart tissue after MI, although it was difficult to determine the morphology of the cells (Online Figure XVII).

**Discussion**

Endoscopic microscopy allowed in vivo time-lapse quantitation and analysis of the number and phenotypes of labeled cells

and their movement and interaction in the heart tissue. Such information cannot be easily obtained with ex vivo histology, which gives only snapshot information at specific time points and specific tissue slices. Compared with whole-body animal imaging, intravital optical microscopy provides much higher resolution and single-cell sensitivity, which is critical to gain mechanistic insights at the cellular level. Recent progress in the ability to suppress the cardiac tissue motion demonstrated the possibility of using intravital microscopy in cardiovascular research in small animals.<sup>17,18</sup> Our work presented here represents a significant technological advance by developing a truly minimally invasive tool that allows high-resolution longitudinal imaging of the heart tissue in mice. Although the maximum imaging depth of fluorescence microscopy is limited to 100  $\mu\text{m}$ , the penetration depth is sufficient to access most of the major coronary vessels and capillaries and the myocardium.

A key enabling technique used in the endoscopic probe is the suction stabilizer. Suction has been widely used for grabbing tissues with minimal damages. It is well known that an excessive suction pressure can cause tissue damage and affect normal physiology.<sup>15</sup> We have found an optimal arrangement using narrow suction tube (2–3 mm in diameter) at adequate pressure levels (50–100 mmHg) and have shown that the optical probe does not cause any significant changes in heart rates and blood flows and does not provoke imaging-induced immune reactions even during repeated longitudinal imaging over several weeks. Furthermore, we have developed a simple method to allow a relatively large tissue area ( $>1\text{ mm}^2$ ) to be scanned, overcoming the intrinsic disadvantage of small-diameter lenses as in the previous demonstrations.<sup>18</sup>

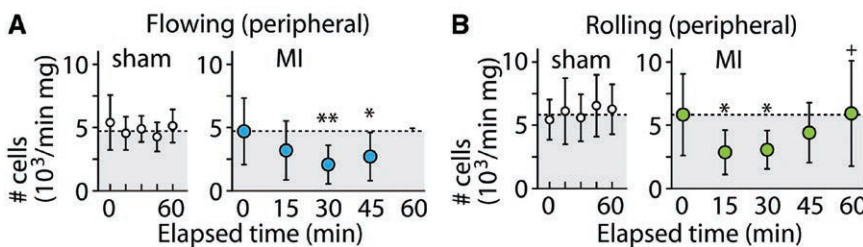


**Figure 7. Flowing and rolling monocytes in peripheral circulation.** **A**, Flux of flowing monocytes in the peripheral circulation, measured in the ear skin after sham operation (left) and acute myocardial infarction (MI; right) animals. **B**, Flux of rolling monocytes in blood vessels in the sham-operated (left) and MI (right) animals. Error bars, SD (n=3–5). \* $P < 0.05$ ; \*\* $P < 0.01$ ; \*\*\* $P < 0.001$  vs 0 min. + $P < 0.05$  vs 15 min.

Imaging through intercostal space is much less invasive than open-heart microscopy previously performed with a standard objective lens or a small-diameter objective firmly glued onto the heart tissue. The fixation of the lens not only limits the FOV to a fixed location but also can cause unwanted biological effects. Thus far, none of the previous techniques allowed repeated, time-lapse imaging of the heart tissue. Our suction-assisted endomicroscopy offers a minimally invasive effective solution, permitting repeated survival imaging. The endoscope can be easily implemented in a commercially available microscope platform.<sup>19</sup>

Using this imaging technique, we have observed an unexpectedly abundant number of patrolling (rolling) monocytes in the native heart in the steady state (Figure 6A and 6D), which had never been reported before. This finding provides direct evidence that there are active immune surveillance mechanisms in the heart. Active immune surveillance in other organs, such as skin, intestine, and lung, that are constantly exposed to antigens and toxins are well known.<sup>15,28</sup> It is rather interesting to find such vigorous patrolling behavior of immune cells in the heart that resides deep inside the body and is protected by physical defensive barriers from harmful extrinsic factors. In fact, we found that the number of patrolling monocytes observed in the steady state was sufficient to account for the rapid increase in the number of monocytes in the infarct within 15 to 30 minutes after acute MI (Figures 5A, 5B, 6C, and 6D).

We also observed a rapid transition of monocytes from rolling to flowing status in the border after the onset of MI (Figure 6C and 6D). Although the detailed mechanism driving this change is unknown, the transition from rolling to flowing monocytes can expedite the infusion of monocytes into the infarct area, and therefore it may be a recruiting mechanism orchestrated by the infarcted tissue. We have shown that the patrolling and flowing monocytes in the blood stream are the first pool of monocytes infiltrating into the infarct immediately after the onset of MI. Considering the significant number of these cells and their potential roles in the critical time after the onset of ischemic injury, we call it a vascular reservoir, distinguished from the well known splenic reservoir,<sup>31</sup> which is activated in a later phase.

In the current paradigm, it is believed that a massive recruitment of neutrophils occurs within a day after MI, followed by the infiltration of monocytes and macrophages, including proinflammatory monocytes with phagocytic and proteolytic functions promoting the digestion of the infarcted tissue and the removal of necrotic debris.<sup>2</sup> Reparative monocytes inducing myofibroblast accumulation, angiogenesis, and the deposition of collagen are known to arrive later.<sup>2</sup> Increased monocyte traffic in acute MI also promotes atherosclerosis.<sup>30</sup> However, little had been known about the inflammatory and reparative responses at earlier stages immediately after MI. Our study, enabled by the minimally invasive suction-assisted endoscope, provided a new insight into the trafficking of immune cells at the onset of acute MI. A timely and balanced immune response orchestrated by monocytes and neutrophils is thought to be crucial for optimal healing of MI. Insufficient or exaggerated recruitment of monocytes could delay wound healing, and delayed infiltration by reparative monocytes

might impair the formation and remodeling of granulation tissue. The early-infiltrating monocytes may actively attract neutrophils to the infarct, as observed in lung inflammation.<sup>32</sup> Our finding of early monocyte infiltration after MI suggests therapeutic strategies based on the swift and selective control of monocyte infiltration.

## Acknowledgments

We thank Mark Myunghwan Choi, Woei-Ming Lee, and Seonghoon Kim for technical help in microscopy and Thomas Graf and Klaus Ley for generous gift of *LysM<sup>sfpr/gfp</sup>* mice.

## Sources of Funding

This work was supported by grants from Massachusetts General Hospital The Executive Committee on Research Postdoctoral Fellowship, National Institutes of Health (U54CA143837, R01AI081734, P41EB015903), and the Ministry of Education, Science, and Technology of Korea (World Class University R31-2008-000-10071-0, 2011-0009503, and WCI 2011-001).

## Disclosures

None.

## References

1. Woollard KJ, Geissmann F. Monocytes in atherosclerosis: subsets and functions. *Nat Rev Cardiol*. 2010;7:77–86.
2. Nahrendorf M, Pittet MJ, Swirski FK. Monocytes: protagonists of infarct inflammation and repair after myocardial infarction. *Circulation*. 2010;121:2437–2445.
3. Anversa P, Kajstura J, Leri A, Bolli R. Life and death of cardiac stem cells: a paradigm shift in cardiac biology. *Circulation*. 2006;113:1451–1463.
4. Chien KR, Domian IJ, Parker KK. Cardiogenesis and the complex biology of regenerative cardiovascular medicine. *Science*. 2008;322:1494–1497.
5. Ieda M, Fu JD, Delgado-Olguin P, Vedantham V, Hayashi Y, Bruneau BG, Srivastava D. Direct reprogramming of fibroblasts into functional cardiomyocytes by defined factors. *Cell*. 2010;142:375–386.
6. Eriksson EE. Intravital microscopy on atherosclerosis in apolipoprotein e-deficient mice establishes microvessels as major entry pathways for leukocytes to advanced lesions. *Circulation*. 2011;124:2129–2138.
7. Lucitti JL, Jones EA, Huang C, Chen J, Fraser SE, Dickinson ME. Vascular remodeling of the mouse yolk sac requires hemodynamic force. *Development*. 2007;134:3317–3326.
8. Miller MJ, Wei SH, Parker I, Cahalan MD. Two-photon imaging of lymphocyte motility and antigen response in intact lymph node. *Science*. 2002;296:1869–1873.
9. Fan Z, Spencer JA, Lu Y, Pitsillides CM, Singh G, Kim P, Yun SH, Toxavidis V, Strom TB, Lin CP, Koulmanda M. In vivo tracking of 'color-coded' effector, natural and induced regulatory T cells in the allograft response. *Nat Med*. 2010;16:718–722.
10. Fujisaki J, Wu J, Carlson AL, et al. In vivo imaging of Treg cells providing immune privilege to the haematopoietic stem-cell niche. *Nature*. 2011;474:216–219.
11. Chilian WM, Eastham CL, Marcus ML. Microvascular distribution of coronary vascular resistance in beating left ventricle. *Am J Physiol*. 1986;251:H779–H788.
12. Greenberg DS, Kerr JN. Automated correction of fast motion artifacts for two-photon imaging of awake animals. *J Neurosci Methods*. 2009;176:1–15.
13. Schroeder JL, Luger-Hamer M, Pursley R, Pohida T, Ched'hotel C, Kellman P, Balaban RS. Short communication: Subcellular motion compensation for minimally invasive microscopy, in vivo: evidence for oxygen gradients in resting muscle. *Circ Res*. 2010;106:1129–1133.
14. Wiesmann F, Szimtenings M, Frydrychowicz A, Illinger R, Hunecke A, Rommel E, Neubauer S, Haase A. High-resolution MRI with cardiac and respiratory gating allows for accurate in vivo atherosclerotic plaque visualization in the murine aortic arch. *Magn Reson Med*. 2003;50:69–74.
15. Looney MR, Thornton EE, Sen D, Lamm WJ, Glenny RW, Krummel MF. Stabilized imaging of immune surveillance in the mouse lung. *Nat Methods*. 2011;8:91–96.
16. Kim P, Tocco G, Kant CD, Benichou G, Yun SH. In vivo fluorescence endoscopic cellular imaging of internal organs in mice. *CLEO/IQEC*. 2009;CMCC4.

17. Li W, Nava RG, Bribrisco AC, Zinselmeyer BH, Spahn JH, Gelman AE, Krupnick AS, Miller MJ, Kreisel D. Intravital 2-photon imaging of leukocyte trafficking in beating heart. *J Clin Invest.* 2012;122:2499–2508.
18. Lee S, Vinegoni C, Feruglio PF, Fexon L, Gorbato R, Pivoravov M, Sbarbati A, Nahrendorf M, Weissleder R. Real-time in vivo imaging of the beating mouse heart at microscopic resolution. *Nat Commun.* 2012;3:1054.
19. Kim JK, Lee WM, Kim P, Choi M, Jung K, Kim S, Yun SH. Fabrication and operation of GRIN probes for in vivo fluorescence cellular imaging of internal organs in small animals. *Nat Protoc.* 2012;7:1456–1469.
20. Jung JC, Schnitzer MJ. Multiphoton endoscopy. *Opt Lett.* 2003;28:902–904.
21. Kim P, Puoris'haag M, Côté D, Lin CP, Yun SH. In vivo confocal and multiphoton microendoscopy. *J Biomed Opt.* 2008;13:010501.
22. Veilleux I, Spencer JA, Biss DP, Cote D, Lin CP. In vivo cell tracking with video rate multimodality laser scanning microscopy. *IEEE J Sel Top Quantum Electron.* 2008;14:10–18.
23. Kim P, Chung E, Yamashita H, Hung KE, Mizoguchi A, Kucherlapati R, Fukumura D, Jain RK, Yun SH. In vivo wide-area cellular imaging by side-view endomicroscopy. *Nat Methods.* 2010;7:303–305.
24. Guizar-Sicairos M, Thurman ST, Fienup JR. Efficient subpixel image registration algorithms. *Opt Lett.* 2008;33:156–158.
25. Jung S, Aliberti J, Graemmel P, Sunshine MJ, Kreutzberg GW, Sher A, Littman DR. Analysis of fractalkine receptor CX(3)CR1 function by targeted deletion and green fluorescent protein reporter gene insertion. *Mol Cell Biol.* 2000;20:4106–4114.
26. Faust N, Varas F, Kelly LM, Heck S, Graf T. Insertion of enhanced green fluorescent protein into the lysozyme gene creates mice with green fluorescent granulocytes and macrophages. *Blood.* 2000;96:719–726.
27. Barretto RP, Messerschmidt B, Schnitzer MJ. In vivo fluorescence imaging with high-resolution microlenses. *Nat Methods.* 2009;6:511–512.
28. Auffray C, Fogg D, Garfa M, Elain G, Join-Lambert O, Kayal S, Sarnacki S, Cumano A, Lauvau G, Geissmann F. Monitoring of blood vessels and tissues by a population of monocytes with patrolling behavior. *Science.* 2007;317:666–670.
29. Imai T, Hieshima K, Haskell C, Baba M, Nagira M, Nishimura M, Kakizaki M, Takagi S, Nomiya H, Schall TJ, Yoshie O. Identification and molecular characterization of fractalkine receptor CX3CR1, which mediates both leukocyte migration and adhesion. *Cell.* 1997;91:521–530.
30. Dutta P, Courties G, Wei Y, et al. Myocardial infarction accelerates atherosclerosis. *Nature.* 2012;487:325–329.
31. Swirski FK, Nahrendorf M, Etzrodt M, Wildgruber M, Cortez-Retamozo V, Panizzi P, Figueiredo JL, Kohler RH, Chudnovskiy A, Waterman P, Aikawa E, Mempel TR, Libby P, Weissleder R, Pittet MJ. Identification of splenic reservoir monocytes and their deployment to inflammatory sites. *Science.* 2009;325:612–616.
32. Kreisel D, Nava RG, Li W, Zinselmeyer BH, Wang B, Lai J, Pless R, Gelman AE, Krupnick AS, Miller MJ. In vivo two-photon imaging reveals monocyte-dependent neutrophil extravasation during pulmonary inflammation. *Proc Natl Acad Sci USA.* 2010;107:18073–18078.
33. Nahrendorf M, Swirski FK, Aikawa E, Stangenberg L, Wurdinger T, Figueiredo JL, Libby P, Weissleder R, Pittet MJ. The healing myocardium sequentially mobilizes two monocyte subsets with divergent and complementary functions. *J Exp Med.* 2007;204:3037–3047.

## Novelty and Significance

### What Is Known?

- Intravital fluorescence microscopy is a valuable tool in basic and preclinical studies using animal models.
- Monocytes seem to be key players in the development of heart failure and infarct healing.

### What New Information Does This Article Contribute?

- A novel combination of a suction system and an endoscope implemented within an intravital microscope allows for the study of cellular dynamics in the beating heart in vivo longitudinally.
- There seems to be a robust population of monocytes with patrolling behavior in the normal heart as a mechanism of immune surveillance.
- A massive infiltration of monocytes occurs in the very early phase after myocardial infarction, and these cells come from the vascular reservoir initially (<15 min) and then from the splenic reservoir.

Intravital microscopy has emerged as a valuable tool in various studies with animal models. However, the cardiovascular disease

research has not readily benefited from this technology owing to lack of effective methods. We have introduced a miniature suction-assisted optical probe that has allowed in vivo longitudinal visualization of the same region in the beating heart over weeks. This breakthrough approach has led to the quantification of flowing and rolling monocytes in normal and infarcted cardiac tissues. This is the first time patrolling behavior of monocytes has been reported in the heart. This work also presents the discovery of an early immune cell infiltration after acute myocardial infarction. We have found that massive monocyte infiltration occurs much earlier than previously thought, and these cells come from the vascular reservoir initially. This finding fills a significant gap in our current understanding and provides new insights into early regulation of inflammation and tissue repair after ischemic heart injury. Our work represents a significant technological advance over other methods for heart imaging points the way to how intravital microscopy can now be used in the study of cardiovascular disease.

## Supplemental Material

### **Endoscopic time-lapse imaging of immune cells in infarcted mouse hearts**

**Running title:** *Jung et al.; Vascular reservoir of early infiltrating monocytes*

Keehoon Jung<sup>1\*</sup>, Pilhan Kim<sup>1,2\*</sup>, Florian Leuschner<sup>3,5</sup>, Rostic Gorbatov<sup>3</sup>, Jun Ki Kim<sup>1</sup>,

Takuya Ueno<sup>3</sup>, Matthias Nahrendorf<sup>3</sup>, and Seok-Hyun Yun<sup>1,2,4</sup>

<sup>1</sup>Wellman Center for Photomedicine, Departments of Dermatology, Harvard Medical School and Massachusetts General Hospital, 55 Fruit Street, Boston, MA 02114, USA

<sup>2</sup>Graduate School of Nanoscience and Technology (WCU), Korea Advanced Institute of Science and Technology, Daejeon, 305-701, Republic of Korea

<sup>3</sup>Center for Systems Biology, Harvard Medical School and Massachusetts General Hospital, Boston, MA 02114, USA

<sup>4</sup>The Harvard-MIT Division of Health Sciences and Technology, 77 Massachusetts Avenue, Cambridge, MA 02139, USA

<sup>5</sup>Current affiliation: Department of Internal Medicine III, University of Heidelberg, Heidelberg, Germany and DZHK (German Centre for Cardiovascular Research), partner site Heidelberg/Mannheim, Heidelberg, Germany

\* Equal contribution

#### **Corresponding author:**

Seok Hyun Yun, Ph.D.

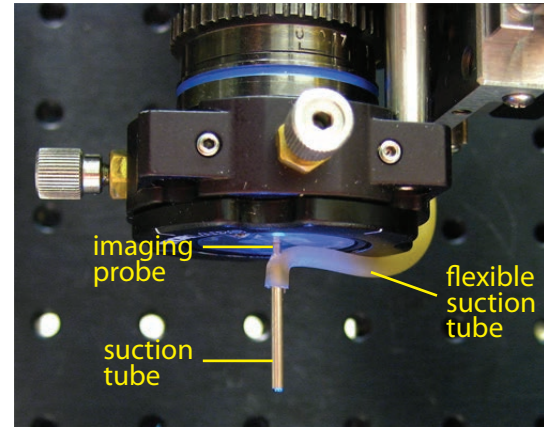
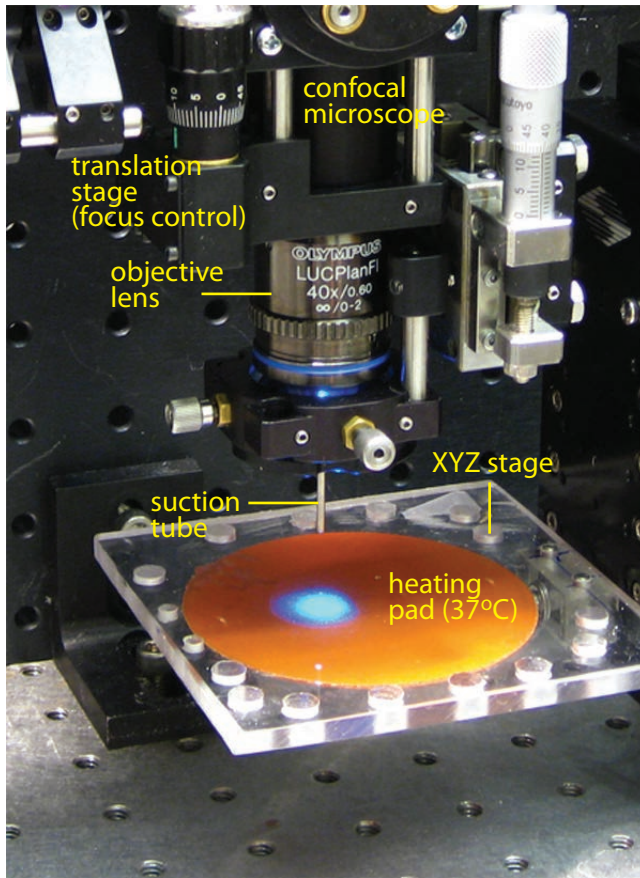
Massachusetts General Hospital and Harvard Medical School

65 Landsdowne St. Rm 525, Cambridge, MA 02139

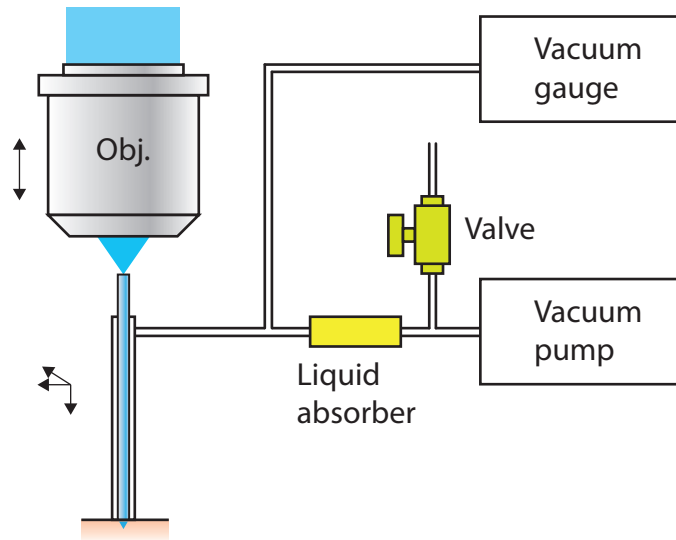
Tel: (617) 768-8704

Fax: (617) 768-8710

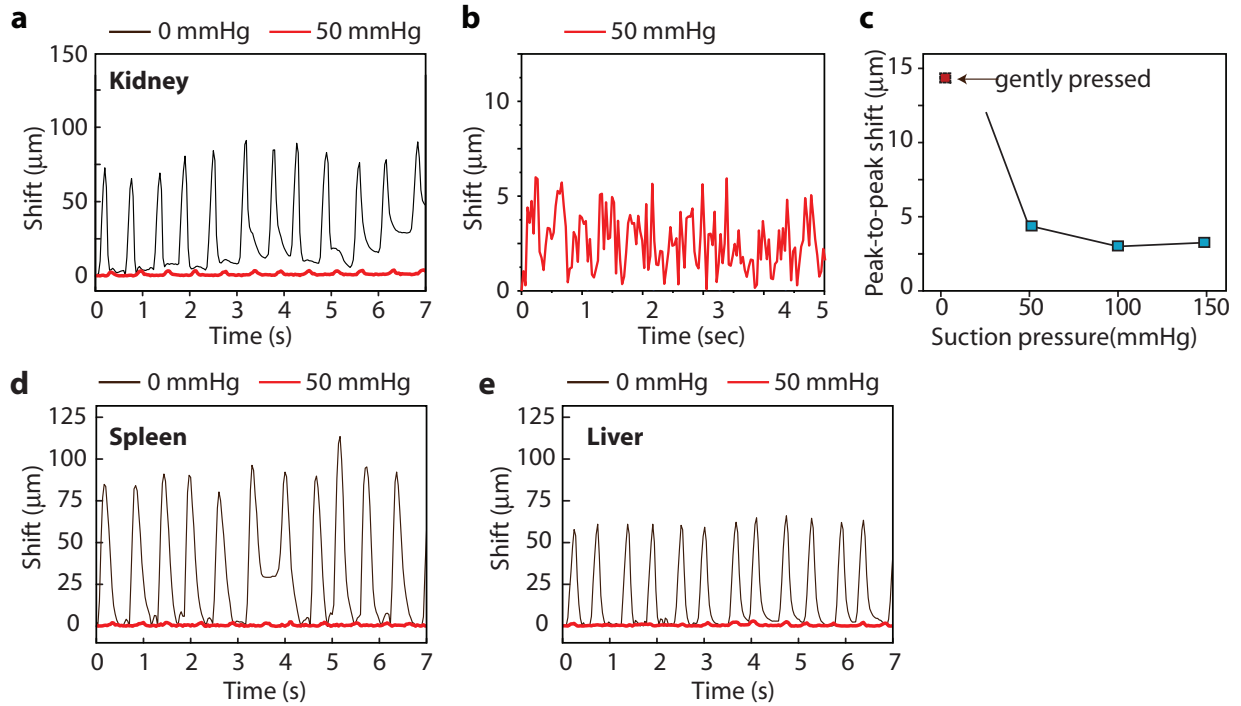
E-mail: [syun@hms.harvard.edu](mailto:syun@hms.harvard.edu)



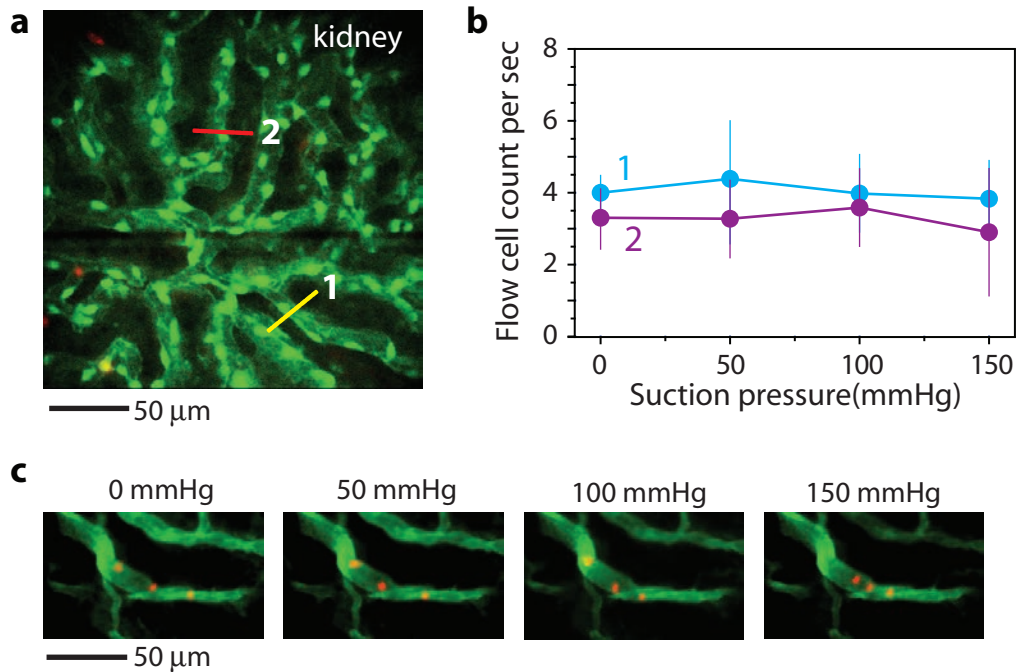
**Online Figure I: Endomicroscopy setup.** The photograph shows an optical probe connected to a miniature vacuum pump via a flexible tube. The probe is integrated into a custom-built video-rate confocal imaging system. The probe consists of an imaging core and an outer suction tube. The core made of triplet graded-index (GRIN) lenses relays fluorescence images to a laser-scanning confocal microscope. The imaging probe provides a subcellular resolution of approximately  $1 \times 1 \times 10 \mu\text{m}^3$ . The imaging core is inserted into the suction tube (O.D. =1.8 mm for the tube shown in the photo) through a small cut made in a flexible rubber tube. The rubber tube is connected to a micro-diaphragm pump for suction. The objective lens (40X, 0.6NA) is mounted on a linear translation stage, so that the distance to the optical probe can be varied. This allows the depth of the focal plane in the tissue to be tuned without moving the endoscope by translating the axial position of the objective lens.



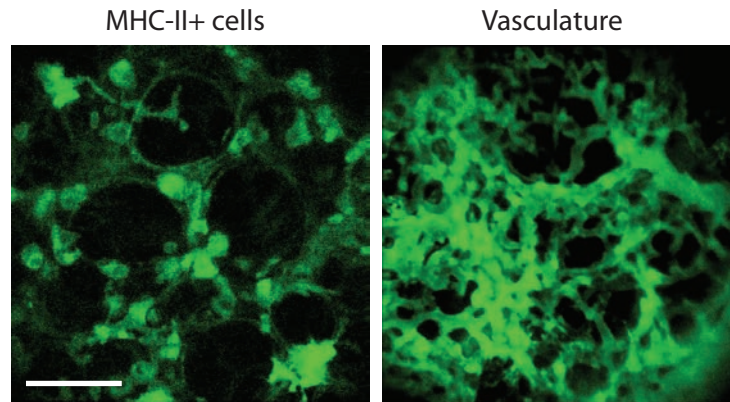
**Online Figure II: Micro-suction system.** The GRIN optical probe is placed inside the suction tube through a latex rubber tube. At the tip of the suction tube, a small amount of epoxy was applied to form an elastic O-ring, which improves the seal and prevents mechanical damage to the tissue in contact. The tube is connected to a miniature diaphragm vacuum pump. A vacuum gauge, flow valve, and liquid absorber are installed to control the suction pressure. The minimum measurable gauge pressure was 20 mmHg.



**Online Figure III: Motion stabilization by suction in various organs.** (A) Tissue movement with (50 mmHg) and without suction (0 mmHg) for motion restriction in the kidney. The periodic motion caused by breathing and heartbeat is observed. The images were acquired after laparotomy at a frame speed of 30 frames per second. The pixel shifts between frames were measured using image correlation algorithm. (B) Tissue movement at 50 mmHg. (C) Tissue motion measured at various suction pressure levels (50-150 mmHg). (D) Tissue movement in the spleen. (E) Tissue movement in the liver.



**Online Figure IV: Effect of suction on the blood flow speed in the kidney.** (A) Image of the kidney of a *Tie2<sup>gfp/+</sup>* mouse. (B) The number of flowing red blood cells per second in the two representative blood vessels (1 and 2) marked in (A) at various suction pressure levels. Prior to imaging, red blood cells were isolated from another mouse of the same strain and stained with Dil fluorescent dye. The labeled red blood cells were intravenously injected into the imaged mouse, and we recorded video from capillaries in the kidney. (C) Assessment of fluorescent beads in a blood vessel in the kidney. Prior to imaging, fluorescent microbeads (red, 0.4  $\mu\text{m}$  diameter) were injected intravenously. The blood vessels were visualized with FITC-Dextran (green). At each suction pressure level, videos were acquired at 30 frames per second. Each image shown is an overlay of three consecutive frames acquired in 0.1 s. The particle flow speed is invariant up to 100 mmHg but is reduced noticeably at 150 mmHg.

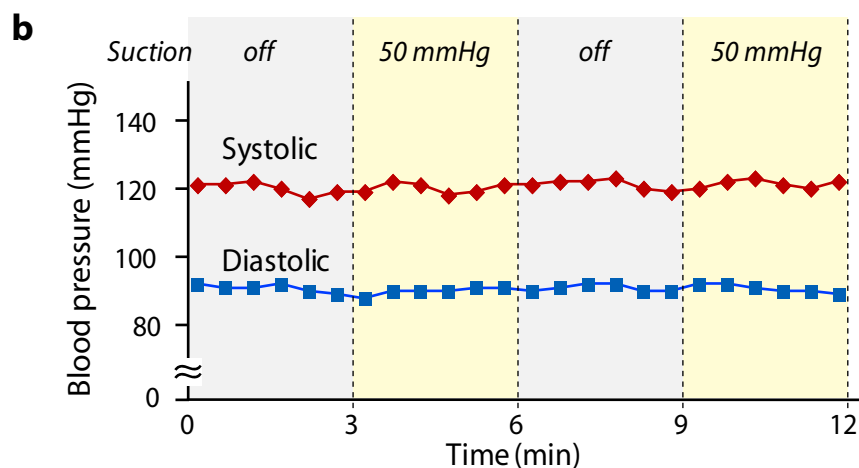


**Online Figure V: Motion-stabilized imaging of the lung.** Images of antigen-presenting cells in a *MHC class II<sup>gfp/+</sup>* mouse (left) and blood vessels (right) visualized by intravenously injected FITC-dextran in the lung. Scale bars, 50  $\mu\text{m}$ .

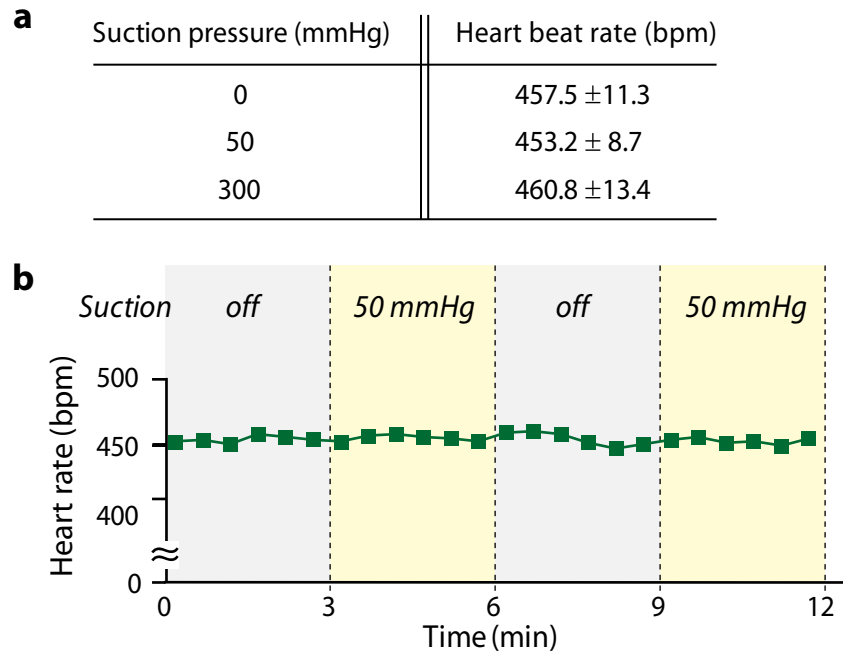
**The effects of the suction on normal physiology (Online Figure VI to IX)** To verify that the local suction of the tissue does not affect the normal physiology of the mouse, we measured arterial blood pressure and heart rates at different suction pressure levels. As shown below, we did not observe any changes associated with suction pressures up to 300 mmHg, five times higher than the typical level used in the experiments.

**a**

Suction pressure (mmHg)	Systolic pressure (mmHg)	Diastolic pressure (mmHg)
0	120.3 ± 3.0	91.2 ± 2.3
50	120.5 ± 3.9	90.0 ± 2.7
300	119.0 ± 3.0	91.4 ± 2.2

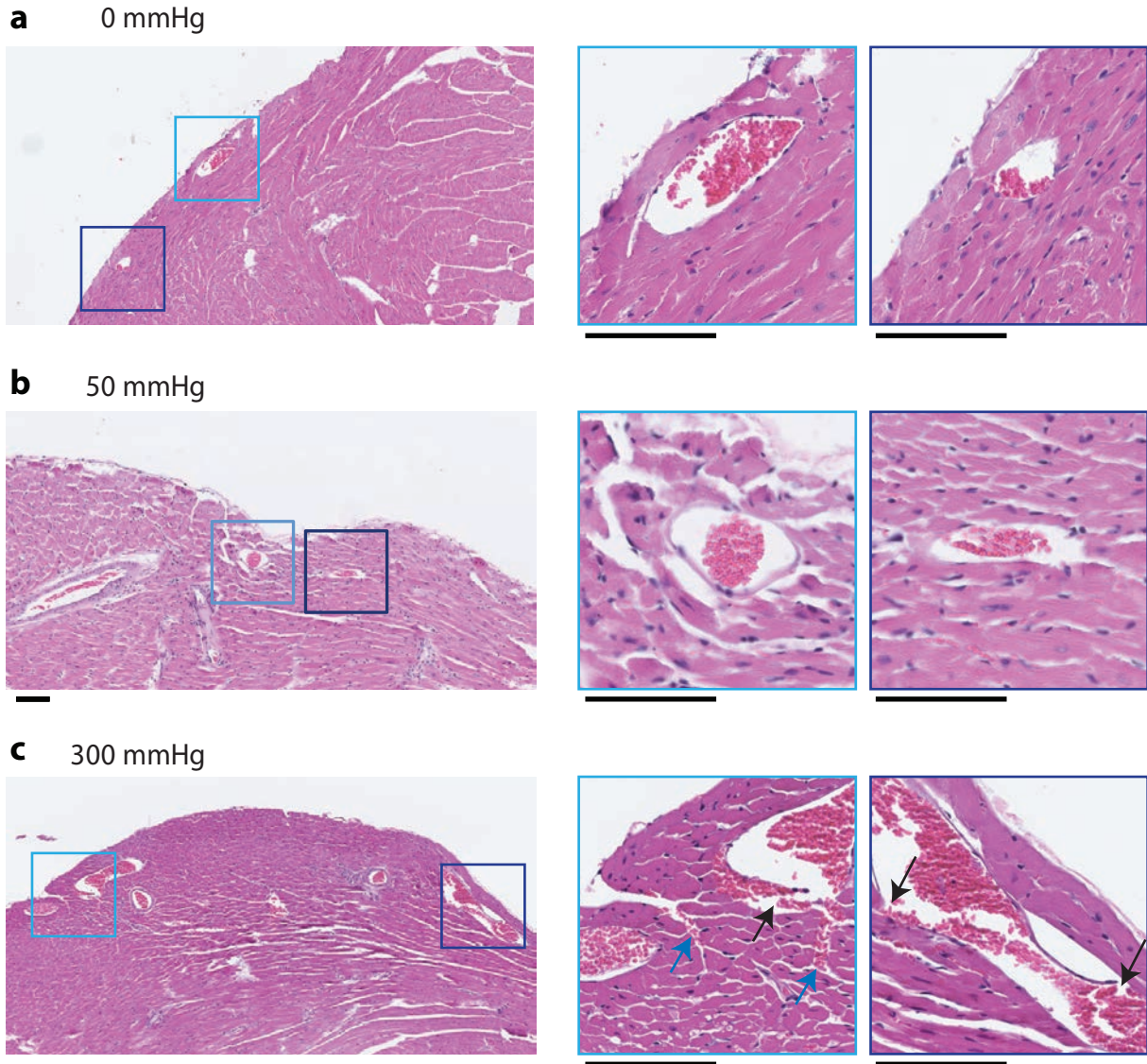


**Online Figure VI: Measurement of blood pressure at different suction pressure levels. (A)** Systolic and diastolic blood pressures at different suction pressure levels. We measured systolic and diastolic blood pressures with a CODA monitor (Kent Scientific, CT) using a volume-pressure sensor with a mouse-tail cuff under our imaging setup with and without suction. Data are reported as mean ± standard deviation. Measurements were performed with four mice (n=4). **(B)** Monitoring of systolic (blue) and diastolic (red) blood pressure when turning the suction pressure (50 mmHg) on and off at 3 min intervals. The arterial pressure traces were not altered by applying the suction pressure on the heart.

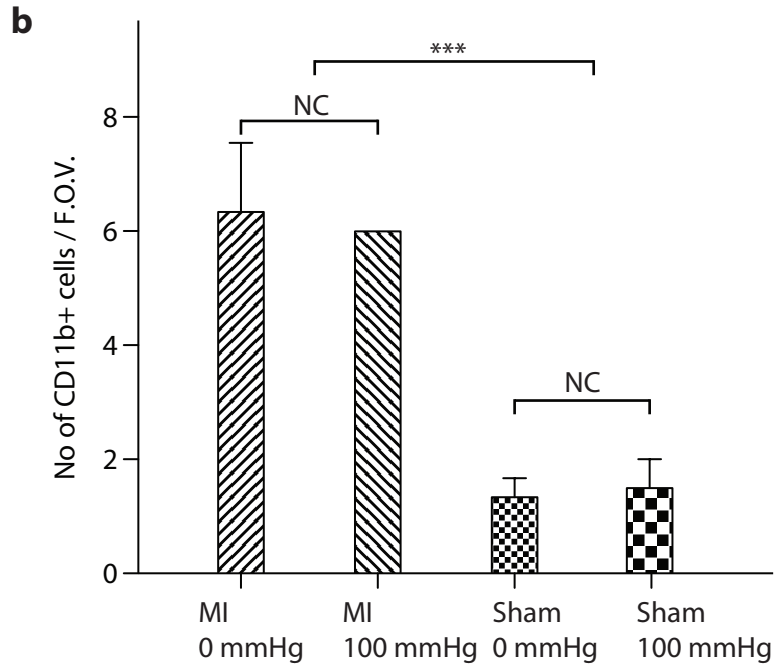
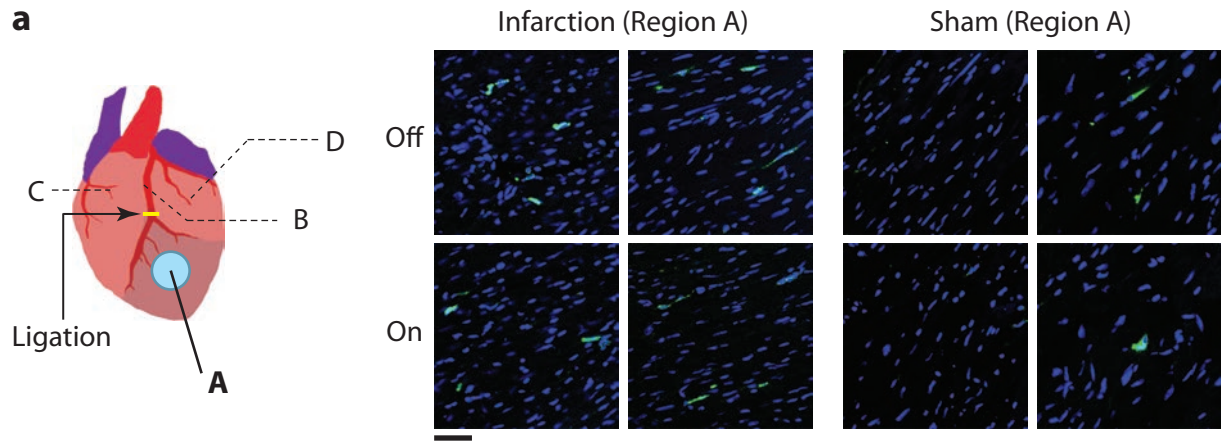


**Online Figure VII: Measurement of heart rate with and without suction pressure. (A)**

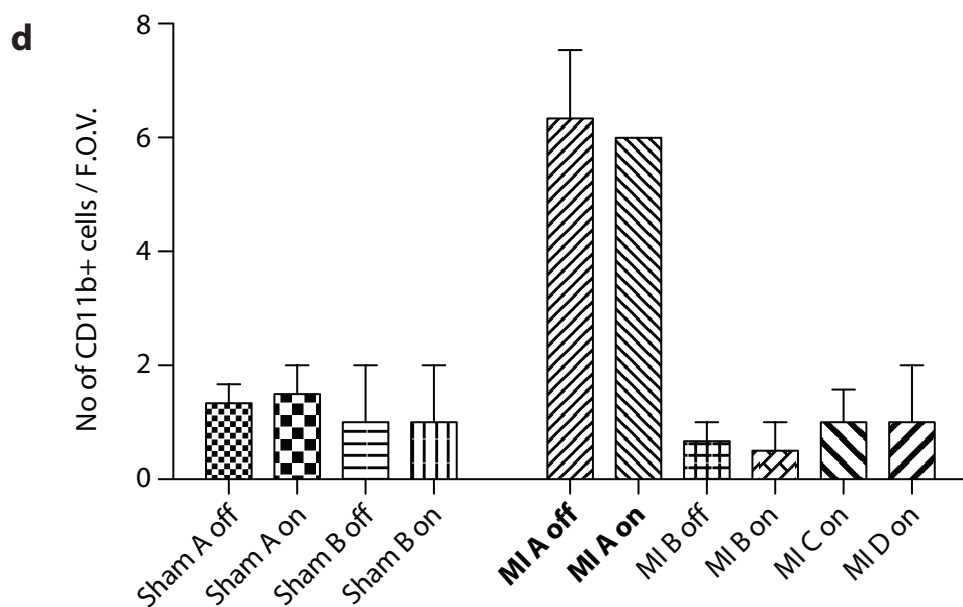
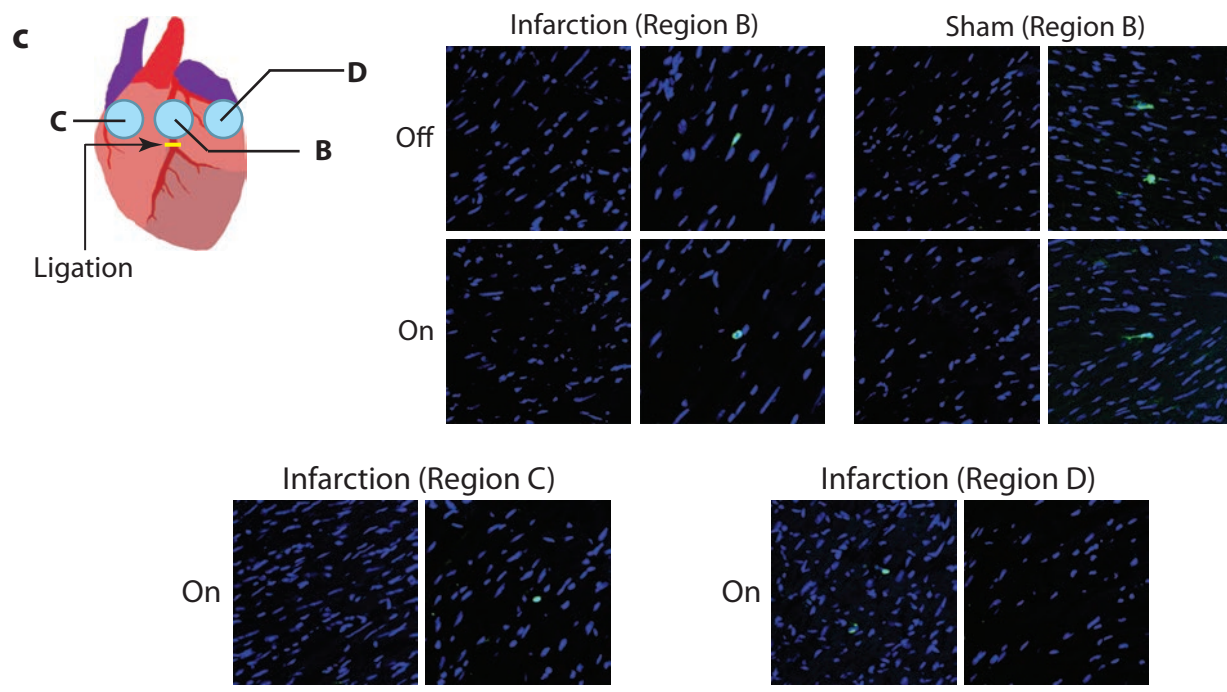
Heart rate at different suction pressure levels. We measured the heart rate with a CODA monitor (Kent Scientific, CT) using a volume-pressure sensor with a mouse-tail cuff under our imaging setup with and without suction. Data are reported as mean ± standard deviation (n=4). **(B)** Monitoring of the heart rate when turning the suction pressure (50 mmHg) on and off with 3 min intervals. The heart rate was not altered by applying the suction pressure on the heart.



**Online Figure VIII: Histological examination of the tissues after suction.** Histology (H&E staining) (A) Tissues harvested from a normal mouse. (B) Tissues after exposed to a suction pressure of 50 mmHg for one hour. Compared to the normal control in A, no indication of tissue damage is observed. (C) Tissues exposed to a suction pressure of 300 mmHg. Blue arrows indicate hemorrhage near the blood vessels. We observe a sign of rupture in some capillary vessels (black arrows) showing a discontinuous endothelial lining and a sign of hemorrhage indicated by the presence of red blood cells (blue arrows) outside the ruptured capillaries. However, even in the extreme condition of 300 mmHg, most of other tissues we have examined appeared normal.

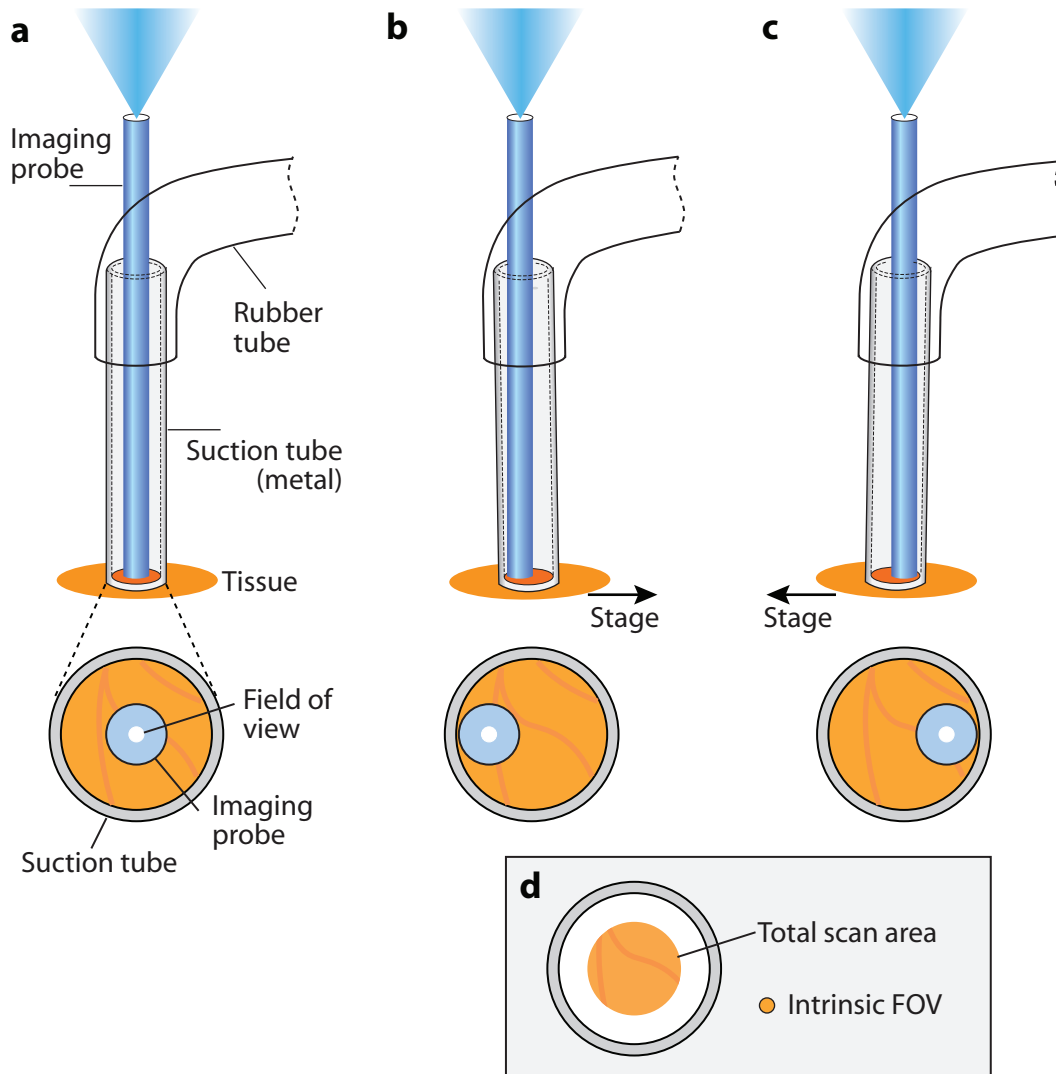


Online Figure IX: (Continued to the next page)



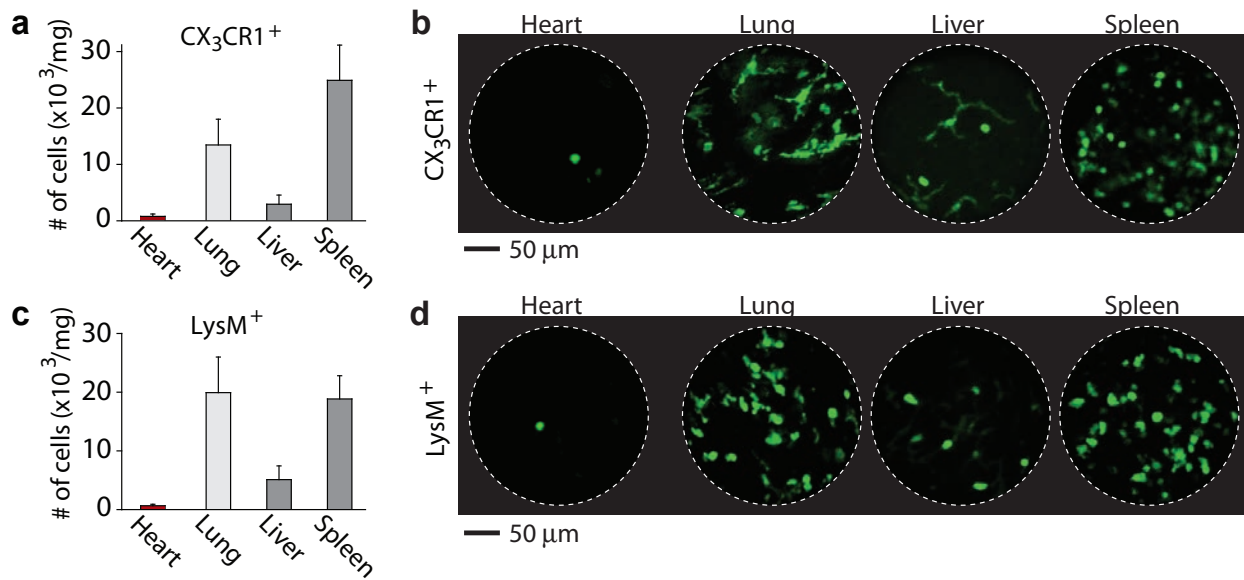
**Online Figure IX: Immunohistochemistry (IHC) analysis of CD11b<sup>+</sup> cells from various regions of the infarcted heart with or without suction.** The tissues were harvested from the control sham-operated and MI mice at 30 min post infarction with (on) or without (off)

application of suction (100 mmHg). The CD11b<sup>+</sup> cells are shown in green and counter stained with DAPI (blue) for visualization of the nucleus. **(A)** Representative images obtained from the region **A** in the schematic of the heart. **(B)** Number of CD11b<sup>+</sup> cells in each group as indicated. There are no differences in the number of CD11b<sup>+</sup> cells between 0 (off) and 100 mmHg (on) suction pressures. Sham-operated control hearts show significantly lower number of CD11b<sup>+</sup> cells regardless of suction. NC, not significant; \*\*\*,  $P < 0.01$  (single-sided student t-test). **(C)** Images obtained from region **B**, **C**, and **D** as indicated in the schematic. **(D)** Number of CD11b<sup>+</sup> cells in each group as indicated. There are no significant differences between 0 and 100 mmHg in the number of CD11b<sup>+</sup> cells in all cases regardless of the location of the heart. This result supports that suction does not induce any inflammatory response. Error bars, standard deviations. Scale bars, 100  $\mu\text{m}$ .

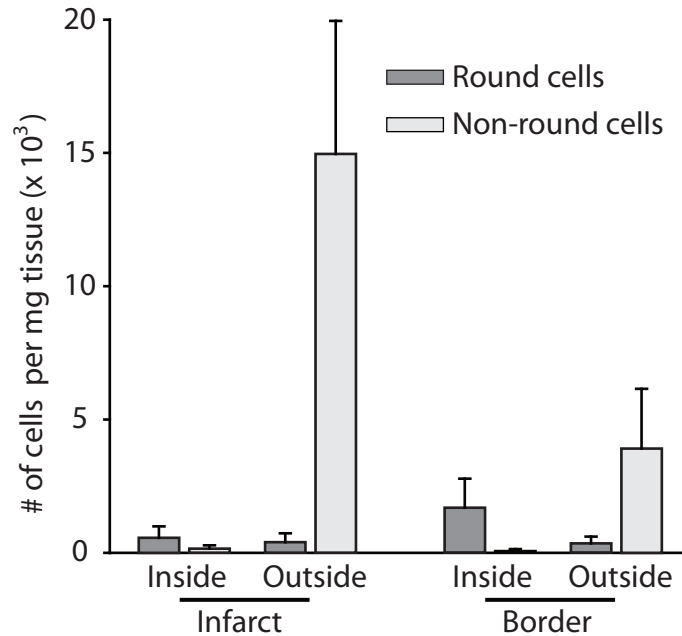


**Online Figure X: Wide-area imaging using suction tube.** (A) Schematic of the probe setup when the GRIN probe is centered in the suction tube. (B) Translation of the imaging probe with respect to the tissue by moving the mouse stage and the suction tube. (C) Translation of the probe in the opposite direction in (B). (D) The total scanned area in comparison to the original field of view (FOV) of the imaging probe. The suction pressure is maintained during translation due to the elasticity of the suction tube material. As the mouse stage is translated in a horizontal direction, the suction tube is tilted at angles of up to  $\pm 2$  degrees, and the imaging probe is slid. This process allows us to view a wide area and to acquire mosaic images. To ensure stable operation, the suction tube has a sufficiently long length (15.2 mm) so that it is easily tilted with a small torque and that the tilt angle is small. The scan area is proportional to the square of the difference between the inner diameter of the suction tube and the outer

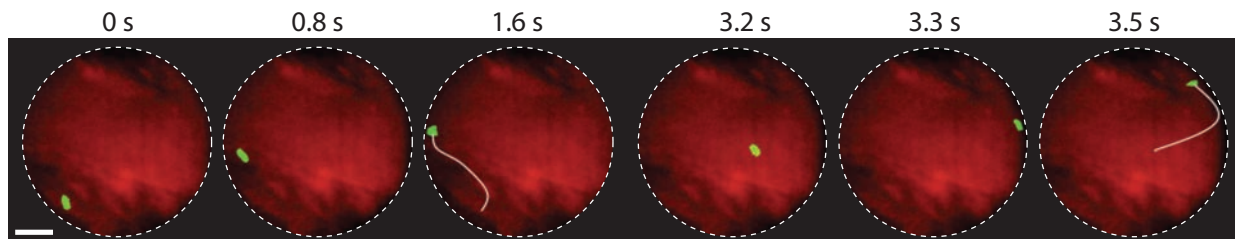
diameter of the imaging probe. The largest tube we used has an inner diameter of 2.7 mm. This device enabled us to scan an area of 1.2 mm x 1.2 mm at a given tube position.



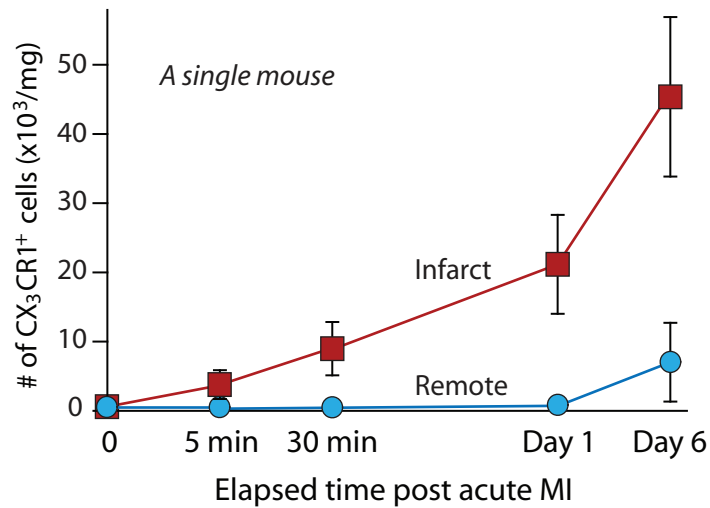
**Online Figure XI. Analysis of various organs in *Cx<sub>3</sub>cr1<sup>gfp/+</sup>* and *LysM<sup>gfp/+</sup>* mice. (A)** The number of CX<sub>3</sub>CR1<sup>+</sup> cells at the cortices of various organs per mg of tissue. **(B)** Endoscopic images of CX<sub>3</sub>CR1<sup>+</sup> cells at various organs *in vivo*. In normal physiological condition, CX<sub>3</sub>CR1<sup>+</sup> cells were found in high density in the spleen and lung but rarely present in the heart. The monocytes in the spleen had roundish morphology, whereas the majority of cells (presumably non-monocytes) in the lung and liver were morphologically irregular. **(C)** The number of LysM<sup>+</sup> neutrophils at the cortices of various organs per mg of tissue. **(D)** Endoscopic images of LysM<sup>+</sup> cells *in vivo*. In *LysM<sup>gfp/+</sup>* mice, the density of neutrophils was also high in the spleen and lung but low in the heart and liver, but most cells had round shapes in all organs.



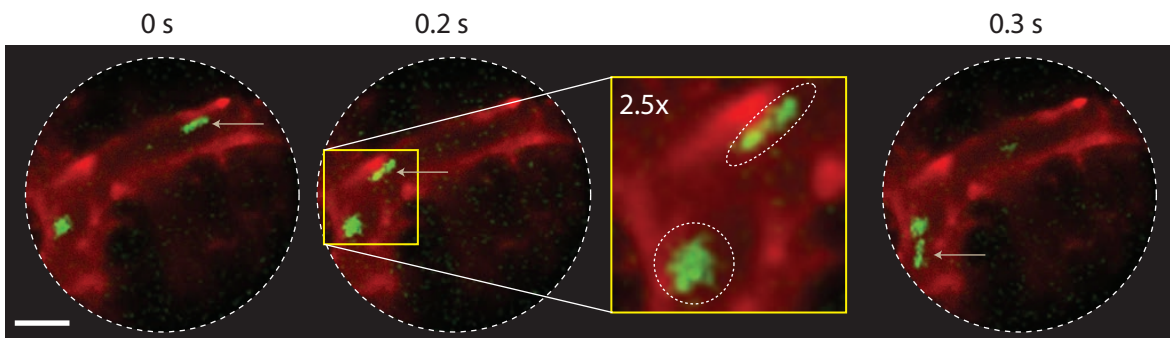
**Online Figure XII: Morphological characterization of monocytes.** Number of round and non-round monocytes inside and outside the blood vessels in the infarct and border areas at 3 hours post MI in *Cx<sub>3</sub>cr1<sup>gfp/+</sup>* mice (n=5). Error bars, standard deviation. A round monocyte was defined as a *CX<sub>3</sub>CR1<sup>+</sup>* cell with an aspect ratio of less than 3:1. The majority of cells in the infarcted area had non-round irregular morphologies. The border area had both irregular cells outside the vessels and round cells inside the vessels.



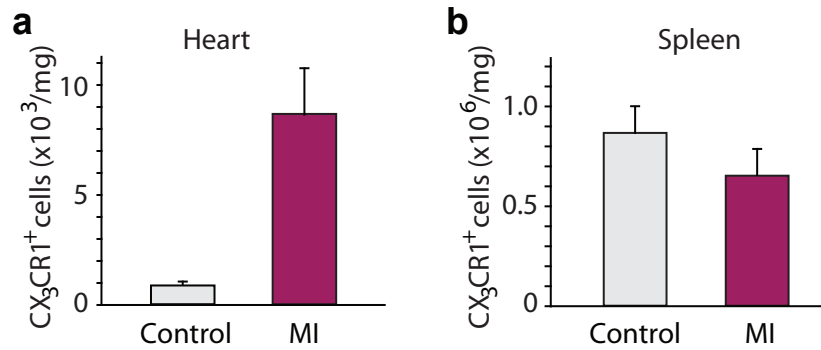
**Online Figure XIII: Flowing cells in the border area after MI.** A sequence of movie frames showing the trace of a *CX<sub>3</sub>CR1<sup>+</sup>* monocyte (green) in the border area. The cells moved along toward a vessel, and once having entered into the vessel, it flows toward the infarct area. These images were taken at 30 min post MI. Scale bars, 50  $\mu$ m.



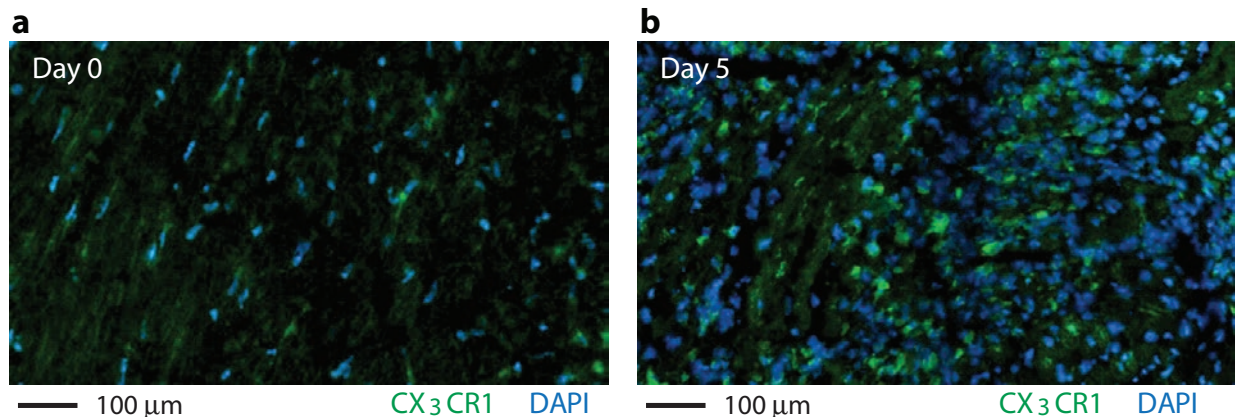
**Online Figure XIV: Longitudinal quantification of CX<sub>3</sub>CR1<sup>+</sup> cells in the infarct and remote areas in a mouse post acute MI.** MI was generated in a *Cx<sub>3</sub>cr1<sup>gfp/+</sup>* mouse by ligating the left anterior descending (LAD) coronary artery. Imaging was performed at day 0 immediately after acute MI, day 1, and day 6 on the mouse. The number of monocytes in the infarct and remote areas was counted in post image analysis. Error bars, standard deviation.



**Online Figure XV: Rod-shaped flowing cells.** A sequence of movie frames showing the trace of a rod-shaped monocyte (green) flowing in the coronary venule, taken from Online Video V. Scale bars, 50  $\mu$ m.



**Online Figure XVI: Supporting flow cytometry data.** The heart and spleen tissues were harvested from control and MI mice with or without suction application (n=3-5). Suction did not affect the results and presented values were derived from combination of suction-applied and non-applied samples. The tissues were digested in enzyme mixture and passed through a cell strainer. The single cell suspensions were stained with the following antibodies: CD11b-APC-Cy7, B220-PE, CD49b-PE, CD90-PE, Ly-6G-PE, NK1.1-PE, Ter119-PE, and F4/80-PE-Cy7 (BD Biosciences). The monocyte subset was identified by CD11b<sup>high</sup> (B220/CD49b/CD90/Ly-6G/NK1.1/Ter119)<sup>low</sup> F4/80<sup>low</sup>. The flow cytometry was performed with a multi-color flow cytometer (FACSAria, BD Biosciences).



**Online Figure XVII: Immunohistochemistry (IHC) analysis of CX<sub>3</sub>CR1<sup>+</sup> cells in the heart with MI.** The tissues were harvested from the control *Cx<sub>3</sub>cr1<sup>gfp/+</sup>* mice (day 0) and from the *Cx<sub>3</sub>cr1<sup>gfp/+</sup>* mice at day 5 post MI (without suction) and were prepared for frozen sections. The CX<sub>3</sub>CR1<sup>+</sup> cells are shown in green and counter stained with DAPI (blue) for visualization of the nucleus. The slides show the increased number of monocytes in the infarcted area post MI,

which is consistent with our in vivo observation. However, IHC is not well suited for analyzing the morphology of cells, the precise location of cells, and the dynamic movement of cells.

### **Supplemental Movies (Online Video I to VI)**

Note: The original raw movie with 512 by 512 pixels per frame was compressed (H.264) and resized to 256 x 256 pixels (or 200 by 200 pixels) per frame to reduce the file size.

#### ***Online Video I: Motion stabilization***

**Online Video IA:** Movie of blood vessels visualized by injecting anti-CD31 antibody conjugated with Alexa 647 in the heart tissue. The intrinsic heartbeat results in significant motion artifacts. The tissue movement is considerably reduced by gently pressing the tissue with the endoscope, but the residual motion causes significant artifacts. At a suction pressure of 50 mmHg, the motion is stabilized within less than 5-10  $\mu\text{m}$ .

**Online Video IB:** Movie of blood vessels visualized by injecting FITC-Dextran in the heart tissue.

#### ***Online Video II: Illustration of the suction-induced force***

In this movie we demonstrate two experiments to illustrate the magnitude of suction force. In the first demonstration, suction was used to pull a thin tape (3M, Inc.). Once the suction tube (O.D. 2.9 mm) makes a steady contact with the tape, the tube pressure is increased to a

predetermined level adjusted by a flow valve. The outer scale in the gauge is in the unit of 10 mmHg (i.e. a number 10 indicates 100 mmHg). The tape is moved by the suction at 60 mmHg but eventually detached from the tube. In the second demonstration, the suction tube was used to pull the skin in the forearm of the operator. As the operator lifts the suction tube away from the skin, the suction force generates only minor stretching of tissue (and no pain to the operator). The movie clips illustrate the relatively weak force by the suction pressure at 50-100 mmHg.

### ***Online Video III: Effects on blood flow***

**Online Video IIIA:** Blood flow in the heart tissue is visualized by intravenously injected anti-CD31 antibody conjugated with Alexa 647. No changes in the flow are seen as the suction pressure is increased gradually from 50 to 150 mmHg.

**Online Video IIIB:** Same tissue area as in Movie 3A. As the pressure was increased to 300 mmHg (in  $t=10-15$  s), the vessel in the middle is apparently flattened, and little flow of the dye is observed. As the pressure was lowered to 50 mmHg, the flow in the vessel is restored to the normal state.

### ***Online Video IV: Illustration of a scanning method***

This movie shows MHC Class-II<sup>+</sup> cells in the heart tissue visualized as the tissue was moved horizontally (first in Y and then in X). A mosaic over a large area was obtained by this scanning method.

### ***Online Video V: In vivo images of CX<sub>3</sub>CR1<sup>+</sup> monocytes inside a coronary venule***

This movie shows crawling, rolling, and flowing monocytes (green) in a coronary vessel (red, TRITC-dextran) in the myocardium of a  $CX_3CR1^{gfp/+}$  mice.

***Online Video VI: In vivo images of  $CX_3CR1^+$  monocytes in the peripheral circulation***

This movie shows a monocyte (green) rolling in a vein (left; flowing from top to bottom) and a flowing monocyte in an artery (right; flowing from bottom to top) in the ear skin at one hour after acute myocardial infarction.